Letter Report
TLR-RES/DE/CIB-CMB-2021-07

CORROSION IN SODIUM FAST REACTORS

May 2021

PREPARED FOR:

U.S. Nuclear Regulatory Commission
TASK ORDER NO. 3131002N0007 (Task 2b)

PREPARED BY:

Oak Ridge National Laboratory
Marie Romedenne
Bruce A. Pint

PROGRAM MANAGERS:

Office of Nuclear Regulatory Research
U.S. Nuclear Regulatory Commission
B. Harris
R. Iyengar

This report does not contain or imply legally binding requirements. Nor does this report establish or modify any regulatory guidance or positions of the U.S. Nuclear Regulatory Commission and is not binding on the Commission.

ORNL/ SPR-2020/1580

Materials Science and Technology Division

CORROSION IN SODIUM FAST REACTORS

Marie Romedenne
Bruce Pint

Date Published:

May 2021

Prepared by
OAK RIDGE NATIONAL LABORATORY
Oak Ridge, TN 37831-6283
managed by
UT-BATTELLE, LLC
for the
U.S. DEPARTMENT OF ENERGY
under contract DE-AC05-00OR22725

CONTENTS

LIST OF FIGURES

LIST OF TABLES

LIST OF ABBREVIATIONS

AISI	American Iron and Steel Institute
ANL	Argonne National Laboratory
APMT	Advanced Powder Metallurgy Tube
ASTRID	Advanced Sodium Technological Reactor for Industrial Demonstration
BCC	Body centered cubic (crystal structure)
BSE	Backscattered electron (images)
CDFR	China Demonstration Fast Reactor
EDS	Energy Dispersive X-ray Spectroscopy
FBR	Fast Breeder Reactor
FCC	Face centered cubic (crystal structure)
FCL	Forced Convection Loop
FM	Ferritic Martensitic (steel)
IHX	Intermediate Heat Exchanger
LCAC	Low-Carbon, Arc-Cast (molybdenum)
LWR	Light Water Reactor
PFBR	Prototype Fast Breeder Reactor (India)
ODS	Oxide Dispersion Strengthened
ORNL	Oak Ridge National Laboratory
PRISM	Power Reactor Innovative Small Module
SFR	Sodium Fast Reactor
SS	Stainless steel
TCL	Thermal Convection Loop
UKAEA	United Kingdom Atomic Energy Authority
UTS	Ultimate Tensile Strength
XRD	X-ray Diffraction

EXECUTIVE SUMMARY

Compatibility of structural materials with liquid sodium is one of the most important aspects of the safety and lifetime of sodium fast nuclear reactors (SFRs). This report reviews relevant and publicly available knowledge on the interaction between sodium chemistry and thermodynamics with structural materials in static and flowing Na conditions. The report begins with a summary of past SFR designs and structural materials that serve as a basis for the development of present sodium-cooled reactors.

Because the corrosion of structural materials in liquid sodium is strongly affected by the presence of oxidizing (oxygen) and carburizing (carbon) impurities, the solubilities of interstitials and major metallic elements in liquid sodium are reviewed. The different systems and sensors used to purify and monitor the sodium chemistry are also presented.

In the next chapters, the corrosion mechanisms in SFRs are discussed. These mechanisms are studied in laboratory and reactor conditions. Laboratory experiments in static or flowing conditions are essential to provide fundamental understanding of the fundamentals of corrosion and mass transfer phenomena because the various parameters involved are either carefully controlled or monitored. However, these experiments are limited in terms of duration of exposure (a few thousand hours). Reactor exposures are indispensable for the detailed understanding of in-service and long-term (thousands of hours) corrosion mechanisms.

The corrosion of pure metals in static liquid sodium and the corrosion of structural materials in static and flowing liquid sodium are reviewed. The detrimental effect of oxygen on the corrosion of austenitic and ferritic steels in liquid is reported. More work is necessary to understand how the interaction between alloy chemistry and sodium chemistry affect the corrosion behavior and lifetime of Ni-based alloys and ceramics.

Carbon as an impurity in the liquid sodium or transferred between materials in the liquid can induce carburization of heat exchangers, structural steels, and control fuel rods in the reactor's core. The effect of carbon is widely reported from complex reactor and flowing sodium experimental conditions between steels. However, additional work is necessary on the carburization behavior of other materials such as Ni-based alloys.

The impact of corrosion on mechanical properties of structural materials is also discussed. Long-term and in-reactor exposures did not reveal a significant impact of oxidation and dissolution on the mechanical properties of austenitic stainless steels. However, carbon was found to affect the strength and ductility of ferritic steels after long-term exposure in liquid sodium. Limited knowledge exists on the effect of sodium exposure on the mechanical properties of Ni-based alloys and ceramics.

The report concludes with a list of knowledge gaps. Corrosion models are available for a few common austenitic steels. However, given the range of temperatures, materials, and designs being considered, modeling appears essential to reduce the amount and cost of experimental work. In general, less prototypical experimental work has been conducted at the correct temperature and sodium chemistry conditions. These knowledge gaps should not be interpreted as absolute barriers to the advancement of SFR technology. They merely represent guidance for future research in preparation for upcoming needs. Their relevance and importance is entirely dependent on the design choices made for each particular reactor concept.

1. SODIUM FAST REACTORS

1.1 INTRODUCTION

To provide reliable and long-term energy supplies, several countries, including the United States, France, Japan, China, India, and Korea, developed or are in the process of developing fast reactors. SFRs are the most promising candidates, as they were studied and developed in the past (1950–1997). SFRs use liquid sodium as a coolant, unlike LWRs, which use water. With the use of sodium, the neutrons produced by the fission reactions are not moderated and higher power efficiencies are achieved (from 50 to 300 MWe for small plants and up to 1,500 MWe for larger plants). Fast neutron reactors are also used for a closed (recycle) fuel cycle, which allows the transmutation of transuranic waste products and high burnup levels (i.e., a longer core life without refueling). Figure 1 shows a common SFR configuration being considered. Encapsulated fissile materials (metallic fuel such a Zr-U-Pu alloy) are inserted in the core, which is filled with purified liquid sodium (T <550°C) that acts as the primary coolant. The heat generated by the reaction is transferred to a nonradioactive liquid sodium intermediate loop, and the steam produced is converted into power by the power generation loop. In the "pool" design shown in Figure 1, the intermediate heat exchanger (IHX) is located inside the core. In the "loop" design, the IHX is outside the core (not shown).

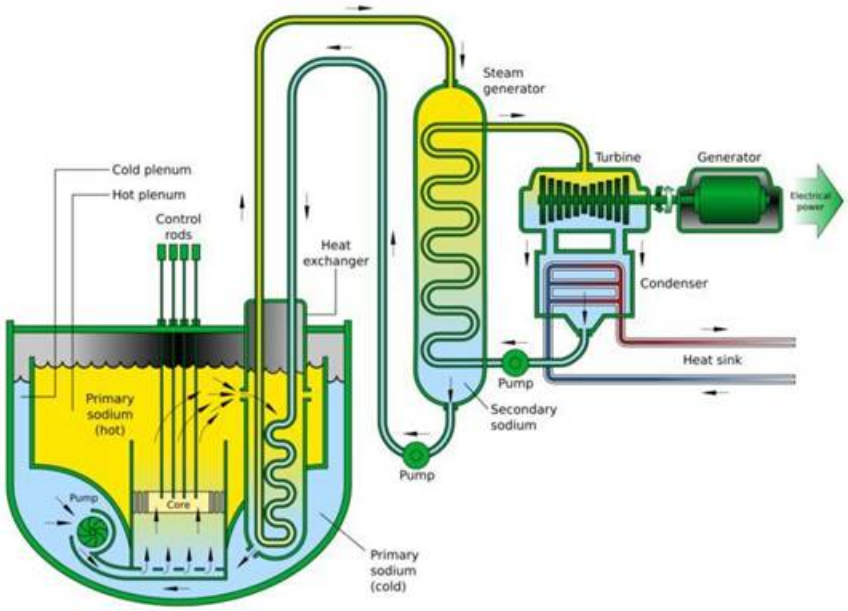

Figure 1. Schematic diagram of a sodium fast reactor with a pool design with the intermediate heat exchanger located inside the core. A secondary sodium loop then heats water to drive a steam generator.

1.2 SFR DEVELOPMENT IN THE WORLD

Several SFR projects have been reported:

- In India, the 500 MWe Prototype Fast Breeder Reactor (PFBR) has a pool design, chosen with a nonradioactive secondary sodium circuit connected to a steam water system. [1]

- In Russia, the BN-800 reactor (800 MWe) is a loop design with independent circulation loops (sodium and water). [2]

- Japan is studying improvements in the Monju reactor maintenance and design. [3]

- In the United States, TerraPower was developing a 500 MWe SFR loop design [4], GE Hitachi Nuclear Energy has developed a 310 MWe reactor known as PRISM (Power Reactor Innovative Small Module) and is now collaborating with TerraPower to build a commercial Natrium Power™ Production and Storage System. [5, 6]

- China is developing the China Demonstration Fast Reactor (CDFR) (600 and 900 MWe). [7]

- South Korea is considering building a 600 MWe prototype SFR. [8]

- In France, a 600 MWe Advanced Sodium Technological Reactor for Industrial Demonstration (ASTRID) prototype pool type reactor was in development until the project was canceled in August 2019. [9]

2. STRUCTURAL MATERIALS

Various materials are used in different systems and components of SFRs. In the next chapters, it will be discussed that corrosion of structural materials is a function of their composition and microstructure as well as the chemistry and temperature of the liquid sodium. Examples of the reported structural and fuel cladding materials for SFRs from different countries are reported in Table 1. Many components are grades of conventional 300 series stainless steels (SS) or 2.25% or 9%Cr steels (Grades 22 and 91). Throughout the report additional alloys will be presented and referred to by their commercial names. Compositions of all investigated materials are reported in Table 2.

Table 1. Structural and core materials for fast reactors (from [10]).

Country	Japan		England	France		Germany	Russia
Reactor name	Monju	JSFR	PFR	Phenix	SPX	SNR300	BN350
Reactor type	Loop	Loop	Tank	Tank	Tank	Loop	Loop
Reactor temperature (out/in) (°C)	529/397		560/399	560/395	545/395	546/377	500/300
Fuel cladding	PNC316 (20%CW) oxide dispersion strengthened		Nimonic PE16	Cr17-Ni13-Mo2.5-Mn1.5-Ti-Si	316L(N)	304	304
Reactor vessel	304	316FR	321	316	316L(N)	304	304
IHX	304	Grade 91	321	316	316L(N)	304	304
Primary pipes	304	Grade 91	–	–	–	304	304
Secondary pipes	304	Grade 91	321	321 304	316L(N)	304	304
Steam generator	Grade 22 321	Grade 91	Grade 22 316 Grade 91	Grade 22 321	Alloy 800	Grade 22	Grade 22

Table 2. Nominal composition of all investigated commercial materials in wt. %.

Name	Fe	Ni	Co	Cr	Mo	Mn	Si	Nb	Al	Ti	C
Nimonic PE16	31	Bal.	2	15–17	2.8–3.8	0.2	0.5	–	1.1–1.3	1,1 – 1.3	0.04–0.08
316	Bal/	10–14	–	16–18	2–3	<2	<0.75	–	–	–	<0.08
316LN	Bal.	10–14	–	16–18	2–3	<2	<0.75	–	–		<0.03
304	Bal.	8–10.5	–	18–20	–	<2	0.75	–	–	–	<0.08
310	Bal.	19–22	–	24–26	<0.75	<2	<1.5	–	–	–	<0.25
321	Bal.	9–12	–	17–19	–	<2	<0.75	–	–	<0.7	0.08
330	Bal.	34–37	–	17–20	–	<2	0.75–1.5	–	–	–	<0.08
Grade 91		0.4–0.5	–	8–9.5	0.85–1/05	0.3–0.6	0.2–0.5	–	0.02	0.01	0.08–0.12
Grade 22	Bal.	–	–	2–2.5	0.1–1.1	<0.6	<0.5	–	–	–	<0.15
Grade 92	Bal.	–	–	8.5–9.5	0.3–0.6	0.3–0.6	<0.5	0.04–0.09	<0.02	<0.01	0.07–0.13
Alloy 800	Bal.	30–35	–	19–23	–	–	–	–	0.15–0.6	0.15–0.6	<0.1
718	–	Bal.	<1	17–21	2.8–3.3	<0.35	<0.35	–	0.3–0.8	0.6–1.1	<0.08
316H	Bal	13.2	–	17.2	2.3	1.9	0.5	–	0.005	0.001	0.06
APMT	Bal,	0.1	–	21.6	2.8	0.1	0.5	0.02	4.9	0.02	0.03
C26M	Bal.	–	–	12.2	2.0	–	0.2	–	6.11	–	<0.01
ODS FeCrAl	Bal.	0.01	–	9.71	–	–	0.02	–	6.03	0.2	0.069
ODS FeCr	Bal.	–	–	12.35	0.95	–	0.03	–	0.02	0.1	0.026

2.1 CORE

For the fuel cladding, austenitic stainless steels 316L and 304 (16–18 % Cr and 8–10 % nickel) are chosen for their good mechanical properties (strength and ductility) and for their relatively good corrosion compatibility with oxygen-purified liquid sodium and with the neutron moderator materials (usually B_4C pellets) at temperatures up to 700°C. In addition, the cladding materials must have low neutron absorption cross-sections and good swelling properties. For that purpose, 316 stainless steels are 20% cold-worked and modified with titanium or silicon additions. Ferritic steels, solid-solution–strengthened nickel-based alloys (PE16) and oxide dispersion strengthened (ODS) alloys are also used for their low swelling characteristics [11].

2.2 REACTOR VESSEL, HEAT EXCHANGERS AND STEAM GENERATOR SYSTEM

The structural materials for the reactor vessel and coolant circuits are chosen in accordance with the American Society of Mechanical Engineers Boiler and Pressure Vessel Code in the United States and with similar codes in Japan and Europe. Ferritic steels (Grade 22) are used for their proven fabricability, weldability, and metallurgical stability with oxygen-purified liquid sodium below 700°C. The ferritic martensitic (FM) modified 9Cr-1Mo steels (e.g., Grade 91) present higher strength and low decarburization in oxygen-purified liquid sodium at the required temperatures and better resistance to stress corrosion cracking [11].

3. SODIUM PROPERTIES AND CHEMISTRY

Liquid sodium being the environment of exposure where corrosion of structural materials of SFRs occurs, understanding of the properties of unpurified and oxygen-purified liquid sodium is necessary.
The thermodynamics and chemistry of sodium in equilibrium with metallic elements present in the reactor's constitutive materials (e.g., Fe, Cr, Ni) and with non-metallic constituents (such as C, O, H, N), that can be present as impurities in liquid sodium, need to be understood and summarized.

3.1 SODIUM PROPERTIES

Sodium properties were reviewed by several authors [12, 13]. As water is commonly used as a coolant in LWRs, the properties of sodium are compared with those of water in Table 3 ([14]). Liquid sodium presents several attractive properties, including a much higher thermal conductivity, a lower specific heat, a lower viscosity, and a longer liquid range than water (Table 3). These better heat transfer properties than water make it a well-suited coolant candidate for SFRs as the thermodynamic efficiency for energy conversion could be increased.

Table 3. Thermophysical properties of liquid sodium and water [14].

Property	Sodium	Water
Melting point (°C)	98	0
Boiling point (°C)	877	100
Density (kg/m^3)	845	997*
Thermal conductivity at 500°C (W·K^{-1}·m^{-1})	68.8	0.67 (at 50°C)
Heat capacity at 773 K (kJ·kg^{-1}·K^{-1})	1.269	1.339 (at 50°C)
Specific heat (J·g^{-1}·K^{-1})	1.23	4.18
Viscosity (centipoise) at 20°C	0.072	1

* corrected value

The boiling point of sodium being relatively low (877°C or 1,156 K) will require pressurized systems and/or the use of condensers. The main concern is the chemical reactivity of sodium especially with water and oxygen. The following exothermic reaction with water releases corrosive compounds and gas products that threaten the integrity and safety of the heat transfer system of the reactor.

$$2Na_{(s)} + 2H_2O_{(l)} \longrightarrow 2Na^{+}_{(aq)} + 2OH^{-}_{(aq)} + H_{2(g)}$$

To identify a potential leak from the primary loop (sodium) that could interact with the intermediate loop (water), the level of hydrogen in sodium is carefully measured [15] and monitored [16].

3.2 COMPOSITION AND PURIFICATION OF SODIUM

The main manufacturer of sodium, Métaux Spéciaux, provides technical-grade sodium with calcium, metallic oxides, and potassium as the major impurities. An electrolysis process is used to obtain the standard grade sodium of the composition given in Table 4 [17].

Table 4. Composition of standard grade sodium (from [17]).

Element	Typical
Na	99.9 %
Ca	350 ppm
K	200 ppm
Ba	< 5 ppm
Fe	< 5 ppm
Cl	< 10 ppm
O	unknown

In SFRs, purification of the sodium is necessary to control the corrosion processes and their effects on the mechanical properties of structural materials. Indeed, impurities such as carbon and oxygen play an important role in mass transfer and other corrosion processes of ferritic and austenitic steels [18]. Even though corrosion in liquid sodium may not compromise the mechanical properties of the thickest structural materials, it is important to reduce the amount of these impurities in sodium to limit the accumulation of reaction products in the reactor. The presence of impurities in sodium can lead to the formation of clusters that can reduce or even block flow in the IHX. For example, in the Japanese Monju reactor, nuclear-grade sodium was recommended, and thus a sodium purification procedure was required. The composition of the nuclear-grade sodium is reported in Table 5.

Table 5. Specification of sodium for Monju (from [17]).

Element	ppm maximum	ppm
O	< 30	< 10
H	< 5	< 1
C	< 30	–
Cl	< 30	–
B	< 4	–
K	< 300	–
Ca	< 10	–
Li	<10	–
U	< 0.01	–

Different systems and sensors are used to purify and monitor the impurity levels in sodium during operation:

- Stainless steel disk **filters** can be used at temperatures above the melting point of sodium. Oxygen particles are less dense than sodium particles and can easily be filtered. This method allows the oxygen level to be lowered to less than 10 ppm. [19]

- **Cold traps** cool sodium to temperatures near its melting point, where soluble impurities will precipitate. [20]

- **Hot traps** purify by gettering or by a foil equilibration method such as Zr foil equilibration for oxygen. [21]

- **Electrochemical sensors** monitor carbon and oxygen levels. [22]

Once sodium is purified, its purity can be altered by contact with ambient air, the dissolution of alloying elements from the structural materials and the introduction of non-metallic impurities (C, N, O) during operation and maintenance. Details of specific operating parameters and procedures are not publicly available.

3.3 SODIUM CHEMISTRY AND THERMODYNAMICS

When a material with a defined chemical composition is exposed to liquid sodium at a specified temperature, velocity, and impurity content, thermodynamics such as phase equilibria can give valuable insight into predicting the reaction products that can form between the alloy and the liquid sodium at equilibrium. The corrosion rate of a material in liquid sodium is then governed by diffusion and interfacial processes in the material and in the liquid sodium at the studied temperature.

3.3.1 Chemical thermodynamics

The corrosion processes occurring between a particular alloy and the liquid sodium of specified composition are driven by thermodynamics (chemical potential gradients between the alloy and the liquid sodium) and kinetics. To predict which elements from the alloy will react with the liquid sodium it is necessary to classify them regarding their stability and kinetics of formation/ dissolution in each media (alloy and sodium). For a given time, temperature, and pressure, the compound that is the most stable and the most rapid to form between the liquid sodium and the alloy will control the corrosion of the alloy in sodium until equilibrium is reached. Dissolution of constitutive elements from the alloy into sodium are presented considering that the kinetics of formation of a compound is usually fast (thus not limiting their formation). Therefore, only thermodynamics govern corrosion of alloys in liquid sodium in this case. For example, the dissolution of element i from the alloy into sodium will occur when the chemical potential of element i in the alloy (μ_i^{alloy}) is higher than its chemical potential in the sodium (μ_i^{sodium}). At thermodynamic equilibrium, both potentials should be equal. The chemical potential is expressed as a function of temperature and activities (Eq. [1]).

$$\mu_i^{phase} = \mu_i^0 + RTln\left(a_i^{phase}\right). \quad 1$$

The activity of element i in a phase (a_i^{phase}) is function of the composition of the phase (alloy or sodium) and the temperature. For a solute *i* in a dilute solution (phase), a_i^{phase} is often simplified using Eq. (2),

$$a_i^{phase} = \gamma_i \frac{c_i}{c_0}, \quad 2$$

where γ_i is the activity coefficient of element i, which is equal to 1 when the i shows ideal behavior in the considered phase, c_i is the concentration of element i in the phase and c_0 is the standard state of the element in a dilute solution. Equation (2) can only be used when the element *i* dissolved from the alloy is in solution in the liquid sodium. However, in most cases, element *i* will not remain in solution but will form a more stable compound with sodium or other impurities.

In most of the studies reported here, only solid solutions were assumed (because the exact value of γ_i is unknown), and Eq. (2) was simplified using Eq. (3); c_0 was assumed equal to 1 mol/L, and c_i was assumed equal to the solubility S_i of the element in sodium and T the temperature.

$$\log(S_i, ppm) = A + \frac{B}{T}. \quad (3)$$

where A and B are fitting parameters. Assuming that only sodium solutions of constitutive elements of alloys are exposed to liquid sodium, extensive studies were performed to evaluate the solubilities of alloying elements in liquid sodium [19].

3.3.2 Carbon and nitrogen solubilities in sodium

The solubility of carbon in sodium was measured by different authors between 350 and 1,000°C, considering acetylide, M_2C_2, or graphite as the standard state for carbon in liquid sodium [23-27]. As reported in Figure 2, different solubility relationships were obtained by the various authors. As the solute species in liquid sodium was not clearly identified experimentally, this could explain the discrepancy. The choice of standard state for carbon in liquid sodium will ultimately affect the solubility value of carbon in liquid sodium at the considered temperature. This will then affect the carbon activity in the liquid sodium.

For example, when graphite is considered as the standard state for carbon in liquid sodium, the solubility of carbon at 600°C, from Ainsley et al., is equal to 4 ppm when graphite forms in liquid sodium [24]. According to Eq. (2), this solubility value corresponds to a carbon activity of a_c= 1 if γ_C is assumed equal to 1. An activity of 1 for carbon in liquid sodium corresponds to strong carburizing conditions. If another compound is formed with carbon in liquid sodium, such as Na_2C_2, the solubility of carbon in sodium will increase (two carbon atoms are needed to form the acetylide). In this case, the activity of carbon in sodium, with respect to graphite, will be higher than 1 in liquid sodium, corresponding to even stronger carburizing conditions. In most of the recent literature, the standard state of the element considered (here carbon) is often not mentioned. This can lead to errors in the evaluation of the solubility value of a particular component in the studied phase (here liquid sodium). This is without considering that carbon can form compounds with dissolved metallic elements from the structural elements of the reactors. This will also affect the value of the solubility of carbon in liquid sodium if the formation of these new compounds is not considered.

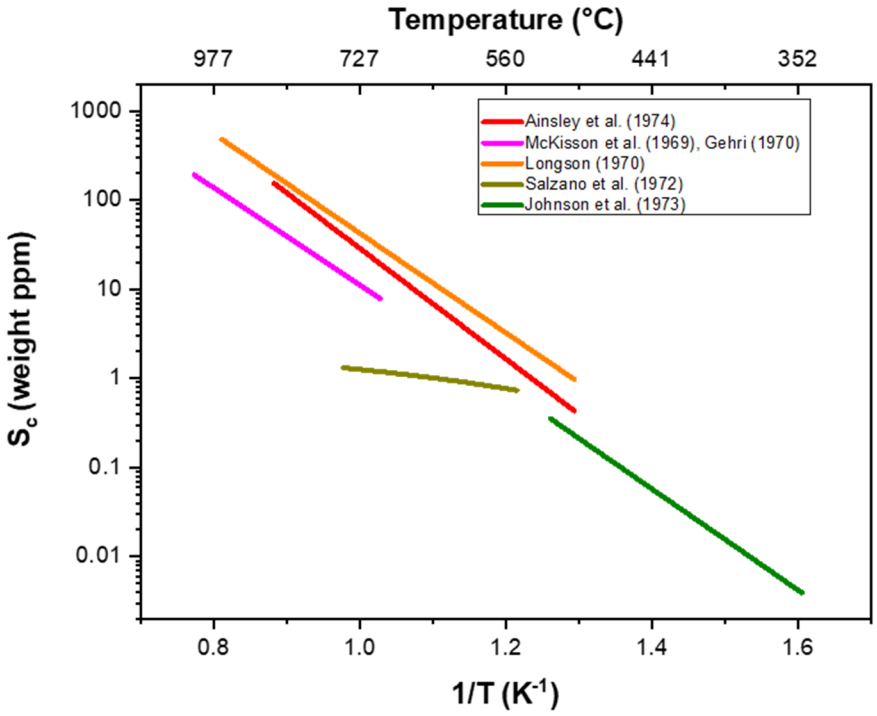

Figure 2. Carbon solubilities in liquid sodium measured by different authors (from [28]).

In contrast to carbon, no compounds have been identified for the Na-N system. Metastable Na_3N may be present and NaN_3 also may form [19]. Regarding the equilibrium for the Na-C-N system, sodium cyanide (NaCN) was observed to dissolve in sodium and to precipitate in cold traps [29].

3.3.3 Solubility of hydrogen in sodium

Above 300°C, hydrogen and sodium form hydrides (NaH). Solid hydrides or gaseous hydrogen dissolves in sodium [19]. The solubility has been measured several times [29, 30]. The two studies measured hydrogen concentrations with different hydrogen meters and produced nearly identical values of the saturation concentrations. Equation (4) shows the solubility relationship:

$$\log(S_H, ppm) = 8.5184 - \frac{3{,}051.3}{T(K)}. \quad (4)$$

3.3.4 Solubility of oxygen in liquid sodium

Solubility data for oxygen in liquid sodium were determined by Noden in the temperature range 114–555°C [31], with significant scatter measured. Equation (5) shows the solubility relationship:

$$\log(S_O, ppm) = 6.239 - \frac{2{,}447}{T(K)}. \quad (5)$$

Although scatter was found between 107 experiments from 5 laboratories, all the groups were thought to have performed careful work, with proper attention to contamination from the atmosphere, accurate measurement of temperature using the equilibration technique, provided that the sodium did not interact

with the container. The scatter could be related to the formation of NaO and Na_2O_2 compounds. as presented in Figure 3.

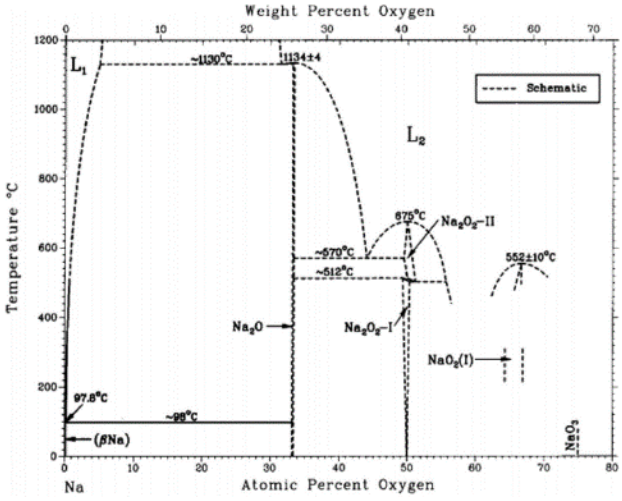

Figure 3. Sketch of the Na-O phase (from [32]).

As previously mentioned for carbon, the presence of metallic elements in sodium can lead to compound formation and complicate the oxygen solubility measurements. Likewise, the presence of oxygen in sodium complicates solubility measurements for metallic elements.

3.3.5 Solubility of pure metallic elements in purified liquid sodium

As presented previously, significant scatter was measured for the solubilities of carbon and oxygen in liquid sodium. This effect arises from the fact that the solubilities of the elements are strongly dependent on the chemistry (i.e., phase stability) in the system (Na-C, Na-O, Na-C-N, Na-C-O). In addition, the solubility of carbon and oxygen can also be affected by the presence of metallic elements present in the liquid sodium which will form compounds with O or C in liquid sodium.

Therefore, to study the corrosion behavior of a pure metal *M* in liquid sodium it becomes necessary to know which compounds will form at thermodynamic equilibrium since the solubility of each considered element will be affected by the formed oxide compound. In pure sodium, the following binary phase diagrams should be used for each element considered:

- M-Na

If sodium contains impurities such as carbon and oxygen, at least the following ternary diagrams should be used for each element considered:

- M-C-Na
- M-O-Na

In the case of a multiphase alloy in contact with commercial liquid sodium containing oxygen impurities, the situation is even more complex. The corrosion of an alloy in liquid sodium will be defined by the stable compounds that can be formed among all of the constitutive elements of the alloy, sodium, and impurities like oxygen. For example, when alloying elements *M* are dissolved in sodium, they can form binary or ternary compounds associated with oxygen or carbon [33] (Eq. [6]).

$$\frac{y}{2}O_2 + xNa + M = Na_xMO_y \quad (6)$$

For example, many oxides can be formed with Cr, Ni, and O. A list of the most commonly observed oxides in sodium is shown in Table 6 with their respective Gibbs energies of formation (ΔG_f^0). The oxides $NaCrO_2$ and Na_4FeO_3 are known to influence the corrosion of steels in sodium [34]. They are formed at ppm levels in sodium. The oxide Cr_2O_3 was not observed to form at any oxygen level in sodium [19].

Table 6. Standard Gibbs energies of formation of sodium oxides [35].

Na_xMO_y	Reference	$\Delta G_f°$ (kj·mol^{-1})	Temperature range (°C)
Na_2O	[36]	−421.5 + 0.1414T	227–1,027
$NaCrO_2$	[37]	−874.6 + 0.20921T	427–827
Cr_2O_3	[38]	−1,109.9 + 0.2472T	Not mentioned
$NaMnO_2$	[38]	−780.8 + 0.1663T	Not mentioned
MnO	[38]	−778.08 + 0.1532T	Not mentioned
Na_2FeO_2	[37]	−777 + 0.20795T	427–827
Na_4FeO_3	[37]	−1,214.17 + 0.34269T	427–827
$NaFeO_2$	[37]	−701.7 + 0.18945T	427–827
Na_2NiO_2	[38]	−640.4 + 0.2217T	Not mentioned
Na_4MoO_5	[38]	−1907.2 + 0.4361T	Not mentioned

Other minor elements such as Co, V, Nb, Mo, Mn Al, W, Zr, and U can also form binary or ternary compounds [19]. The ΔG_f^0 for these compounds were not included in this report. However, numerous ternary phase diagrams among sodium, alloying elements, and oxygen are available elsewhere [19].

In considering the dissolution of multiple elements in sodium, combined with impurities present in the liquid, it is important to be aware of the sodium chemistry at equilibrium. Therefore, to evaluate the dissolution behavior of alloys in liquid sodium, a combined thermodynamics and kinetics approach is necessary. Furthermore, as the temperature is not homogeneous in a reactor, activity values will vary in a thermal gradient. Usually, elements are dissolved from the higher-temperature regions (zones where the chemical potentials of the alloys are higher than in sodium) and are precipitated in the lower-temperature regions (where the chemical potential of the element in the alloy is lower than in sodium). In a circulating system, this mass transfer process of dissolution and precipitation [39] is considered using thermodynamic and kinetic approaches to evaluate the compatibility of structural materials in liquid sodium. Selected solubility measurements are shown in Figure 4.

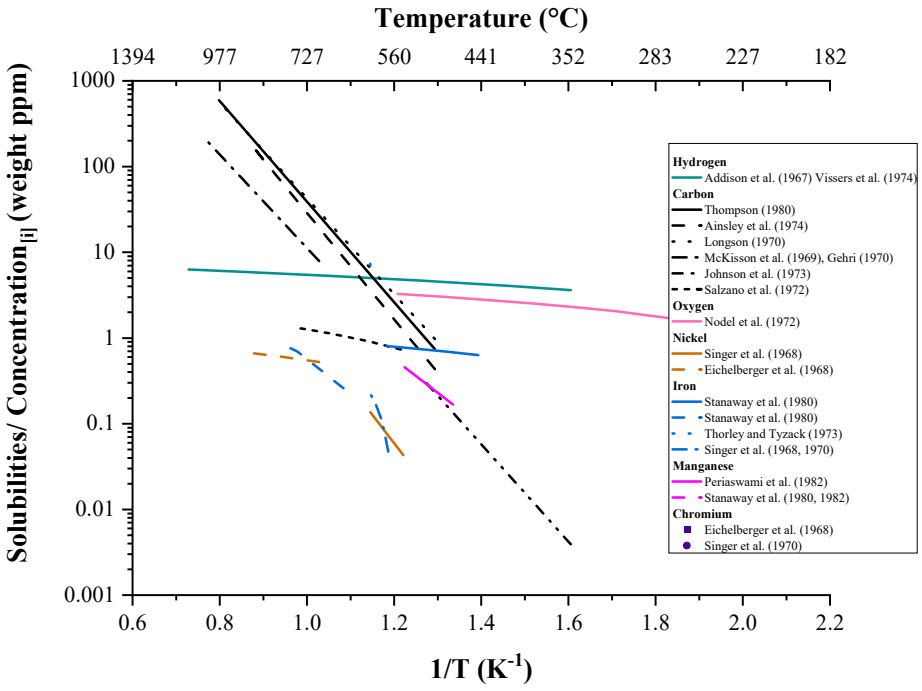

Figure 4. Summary of measured solubilities in the literature. Experimental conditions (oxygen, carbon concentration in Na, temperature, and experimental setup are presented in each reported reference)

Conclusions:

- Solubilities of carbon, oxygen, and metallic elements were reviewed. Although scatter was found between experiments, it is considered that all groups reporting solubilities have done careful work, with proper attention to contamination from the atmosphere, accurate measurement of temperature. Differences were found to be due to the nature of the considered solute species in liquid sodium which was not always the same (for example O concentration in Na) or in other cases not clearly identified experimentally (for example, oxide compound with sodium, carbide compound with sodium).

4. CORROSION MECHANISMS IN SFRs

The corrosion mechanisms of structural materials in liquid sodium can be separated into two categories. The first mechanism category is the dissolution and mass transfer of constitutional elements from the materials into the liquid sodium. The second category involves impurity and interstitial reactions, alloying, and compound reduction [40]:

Dissolution of structural materials in liquid sodium was intensively studied in the past [18, 41-57]. These studies demonstrated reasonable dissolution rates of different steels (austenitic, ferritic, or ODS) in liquid sodium with low oxygen contents [10, 50, 52, 53]. The extent of dissolution in purified sodium and its effect on the mechanical properties of structural materials is considered in the 40-year lifetime design of SFRs, taking into account wall thinning and loss of strengthening elements. Since longer (60 year) lifetimes are expected for future SFRs with higher safety levels, better understanding of the corrosion

phenomena may be needed. The ability to predict the chemical compatibility of a fuel cladding with liquid sodium, when new materials are being introduced (common steels, ODS or new candidate materials), supported by well-chosen experimental observations, could be of great use in identifying suitable materials for specific conditions. Knowledge of the effects of transient or accidental conditions on the chemistry of liquid sodium, and on the corrosion rates of structural materials—as well as the ability to predict the dissolution rate as a function of material composition, thickness, and time—would be useful for designers, operators, and regulators.

The second category of impurity corrosion mechanisms refers to the interaction of the structural materials with elements such as carbon in the sodium. During the dissolution step, carbon is released from other structural materials in liquid sodium [58] or is present in liquid sodium as an impurity (see Section 3.2). Very small (ppm) concentrations of oxygen or carbon can change their potential in liquid sodium. Two different mechanisms can operate in liquid sodium. The first process is the loss of carbon from the structural materials (decarburization). Decarburization releases carbon into the sodium, which then facilitates additional reactions [59, 60]. Carbon is then transported from regions with higher carbon potential to locations with lower carbon potential. The opposite process, carburization, is also well documented [28, 47, 52, 58, 61-67]. Again, the carbon source may be from the decarburization of structural materials or the presence of carbon impurities. For example, the carburization of control rods may be induced by the release of carbon from B_4C components. Carburization is a concern, as it affects the mechanical properties of components [47, 61, 68].

In this section, experimental techniques used to study corrosion in liquid sodium, along with corrosion mechanisms observed in SFRs, are summarized. In addition, a review of the literature regarding the compatibility of structural materials with liquid sodium and its impurities is presented. Finally, the effects of the corrosion mechanisms (dissolution, mass transfer, and carburization/decarburization) on the mechanical properties of structural materials are discussed.

4.1 EXPERIMENTAL TECHNIQUES

4.1.1 Static sodium corrosion test

The first category of corrosion test is called “static” corrosion experiments because sodium is inserted in a closed reactor [52, 69] or in a capsule or crucible [70]. The material of the container should be inert with respect to sodium corrosion. In initial studies [70], nickel capsules were used and sealed in stainless steel vessels. After compatibility issues were identified among nickel, iron, or stainless steels in sodium [34], Mo crucibles were selected [69] because of their good compatibility with sodium and oxygen [71]. However, the introduction of carbon into the system was observed to lead to the formation of Mo_2C. Thus, Mo containers could be problematic for studying dissolved carbon in sodium. Figure 5 and Figure 6 show schematics of typical static sodium experiments. In the sodium–molybdenum capsule experiment illustrated in Figure 6 (used at Oak Ridge National Laboratory (ORNL) for many decades [72]), the outer stainless steel capsule provides secondary containment during the thermal exposure and prevents the Mo from oxidizing and/or evaporating in an oxidizing environment. The capsule is inverted at the end of the exposure to allow the sodium to drain away from the specimen for easier extraction. Similar capsules are used for molten salt corrosion studies [73, 74]. Because of the relatively small (~10-12 cm^3) volume of sodium in each capsule, saturation of a dissolving element X during the corrosion experiment can occur after prolonged exposure. As the concentration of X approaches saturation during exposure, the corrosion kinetics will slow down and can then stop once equilibrium (saturation) is reached between the studied alloy and the liquid sodium. Therefore, static experiments can act as a screening tool for compatibility but are not conclusive, especially in long duration experiments, because of the potential for saturation to affect the result.

Assuming the activity (a_i) of an element is equal to its solubility in liquid sodium (C_i), as mentioned in Section 3.3.1, the dissolution of element i in liquid sodium can be written according to Eq. (7):

$$J_i = k_i(C^S_i - C_i)\,, \qquad 7$$

where J_i is the flux of species i (e.g., Cr) into the liquid, k_i is a constant, C^S_i is the solubility limit of i in the liquid salt, and C_i is the instantaneous concentration of i in the liquid [75]. Thus, as i dissolves into the liquid in the capsule, the reaction should slow and stop as the liquid becomes saturated with i. This is the reason for specifying a preferred ratio higher than 10 between the sodium volume and the specimen surface area in an isothermal capsule test. Furthermore, long-term crucible or capsule tests are limited in value. However, they can be employed as screening tests and for short-term exposures (times ≤2000 h).

From Eq. (7), the rate of mass loss should decrease with time until the concentration of the element i reaches its solubility in liquid sodium, where J_i is equal to 0. For example, the dissolution of iron from the alloy will stop when $Fe_{(s)}$ precipitates in sodium. By selecting materials containing elements with low solubilities (chemical potentials) and low solution rate constants, the dissolution process can be minimized. However, as noted previously, if oxygen is present in sodium, iron can form ternary compounds in sodium (e.g., Na_4FeO_3), resulting in increased solubility of iron in sodium compared with the solubility in the presence of $Fe_{(s)}$ only (i.e. low O levels in the Na). Furthermore, the temperature in SFRs is not homogeneous (the liquid sodium used as a coolant is lower in temperature than sodium present in the core). Thus, different solubility (chemical potential) levels can be achieved in the sodium circuit, resulting in different solubilities (chemical potentials) and solution rates k_i in the sodium circuit. Solution rates k_i will also be affected if dissimilar materials are present in an SFR. Different solubilities (chemical potentials at equilibrium) between each alloy and the liquid sodium will be obtained at different locations in SFRs.

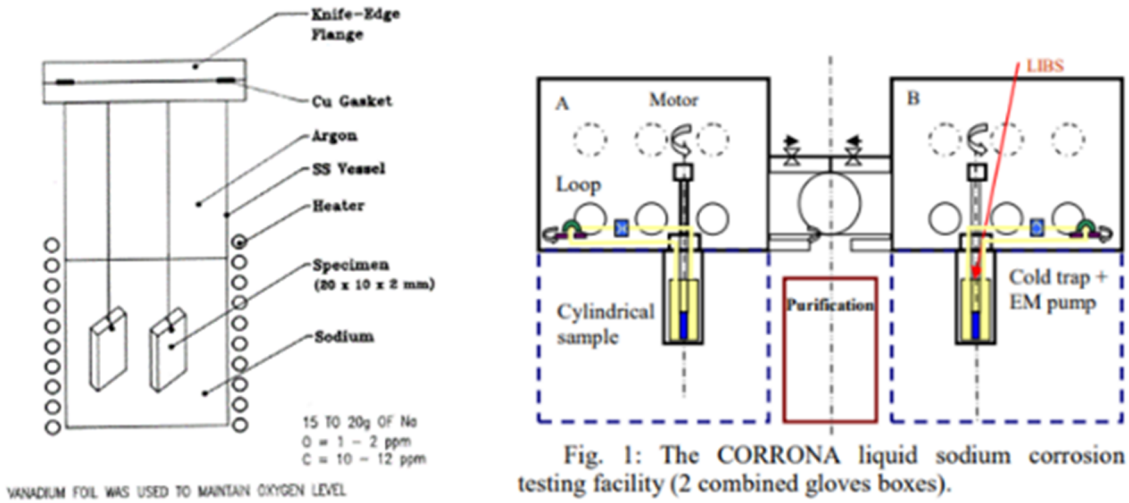

Figure 5. Static sodium experimental setup from [52, 69].

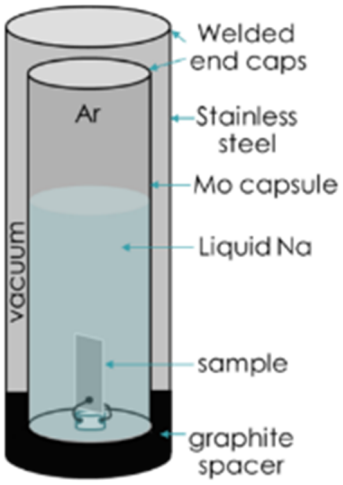

Figure 6. Static sodium experimental setup used for more than 60 years at ORNL.

4.1.2 Flowing sodium corrosion experiments

In static sodium, the corrosion rates are relatively small and often not representative of reactor conditions with temperature gradients [34]. Therefore, convection loops are used. There are two types of convection loops: natural or TCLs and pumped or FCLs. From an engineering perspective, corrosion rates in controlled-velocity FCLs are closer to those measured in reactors. However, without pumps and valves, TCLs are much less expensive to build and operate, but still enable study of the effects of thermal gradients, dissimilar materials interactions, and mass transfer in general [39].

4.1.2.1 Thermal convection loops

Results from TCLs have been reported by many organizations [67, 72, 76]. In a TCL, a section of the loop is heated at the temperature of interest (hot leg) and the other section is not heated or is actively cooled (cold leg) to create the desired temperature gradient. In this experimental setup, flow is driven by the temperature-induced density difference. The temperature gradient also creates a difference in solubility that can drive mass transfer between the two legs. The velocity in a TCL is typically much slower than in-reactor applications, 1–2 cm/s. After operation, the TCL tubing can be sectioned to study the mass transfer, or chains of specimens can be hung in the flow path to measure mass change on each specimen as a function of temperature and location in the hot and cold legs. The mass transfer mechanism is much easier to understand if the specimen materials exposed in the loop are identical to the material of the loop itself, i.e., it is a monometallic TCL. However, materials of interest are not always readily available in tube form to build a TCL. If the TCL loop and specimen materials are dissimilar, chemical potential gradients among the different loop materials will play a role in the observed corrosion behavior. In the literature, it is common to see TCL (and FCL) studies that consider a loop consisting of a material different from the inserted studied coupons [49, 53, 54, 77-81].

4.1.2.2 Forced convection loops

Corrosion of materials is also studied in FCLs, where sodium is mechanically or electromagnetically pumped at a desired velocity [82]. Typically, FCL experiments can explore temperature gradient and velocity effects with conditions comparable to those in SFR designs. However, as noted in the previous section, the FCL may be constructed of multiple materials or expose specimens of multiple materials, complicating the results. Active impurity controls are needed to produce optimal and reproducible results.

4.2 CORROSION OF PURE METALS IN STATIC SODIUM (ISOTHERMAL CONDITIONS)

In static liquid sodium, dissolution of pure metals or structural materials is controlled by thermodynamics (chemical potential gradients between the alloy and sodium) and kinetics [43] as noted in Section 3.3. The dissolution of one element in sodium can be favored by its thermodynamic solubility in sodium, and yet not occur if the kinetics are too slow. To understand the dissolution mechanism in liquid sodium, it is necessary to evaluate which compounds are stable compounds that form at thermodynamic equilibrium between sodium and the alloy. Then kinetics play their role when the slowest reaction controls the dissolution process.

In other words, when the temperature in the reactor is homogeneous and no impurities are present in the liquid sodium, the rate of mass loss of an element *i* (J_i in mol·m^{-2}·s^{-1}) is controlled by the difference between the chemical potential of the element *i* in the alloy (μ_i^{alloy}) and the chemical potential of the element *i* in the liquid sodium (μ_i^{Na}). Typically, μ_i^{alloy} is approximated to be equal to its solubility (S_i in mol·m^{-3}) in liquid sodium assuming a pure element *i* dissolved in sodium at thermodynamic equilibrium. The μ_i^{Na} is approximately equal to the measured concentration of element *i* in liquid sodium ($C_i(t)$ in mol·m^{-3} with *t* as time) [40]. However, as noted previously, this approach can be misleading if compounds are formed between sodium and the solute.

For multicomponent alloys, the dissolution of different elements of the alloy will occur according to the thermodynamics between the alloy and liquid sodium and their kinetics of dissolution. According to Weeks et al., the measured corrosion rate represents the net sum of the rates of each of the many reactions continuously occurring in the system as the reactants attempt to reach simultaneous equilibrium [43]. To understand how corrosion of a multicomponent alloy occurs in liquid sodium, first, it is necessary to review the literature on corrosion of pure elements in static and isothermal liquid sodium.

The corrosion of pure elements in liquid sodium is widely reported in the literature. The corrosion of pure Zr, Ti, Nb, and Ta in liquid sodium containing up to 12 wt. % of oxygen was studied at 500, 550, and 600°C for durations of up to 576 h (24 days) in nickel crucibles. The corrosion products were characterized using x-ray diffraction (XRD). After exposure, ternary and quaternary oxides (Na_3NbO_4, Na_3TaO_4 Na_4TiO_4) were formed at the surface of the metal exposed to liquid sodium containing oxygen [70, 83, 84]. These products led to the embrittlement of the transition metals (which all have high O solubilities). It was also mentioned that the oxidation products might be washed away during the cleaning procedure for the samples if care was not taken [67].

The corrosion of pure metals such as chromium and iron was investigated after exposure to liquid sodium containing up to 6 wt. % oxygen at 600°C [34]. This study aimed to explain the variation in solubility measurements observed in the literature for iron or chromium in liquid sodium. The authors explained that a compound could form between iron or chromium and sodium and result in an increase in the apparent solubility. The corrosion products were characterized using XRD without washing the samples with alcohol or aqueous solvents after 168 h (1 week) and 336 h (2 weeks) at 600°C in sodium containing between 20 ppm and 6.2 wt. % oxygen. The results identified $NaCrO_2$ and Na_4FeO_3 corrosion products at the surfaces of chromium and iron, respectively.

The corrosion of Mo and W was studied in static liquid sodium containing 1 and 3.5 wt. % oxygen and carbon doped sodium (addition of charcoal or titanium carbide or steel tab), respectively, for periods of 48–576 h and temperatures between 400 and 650°C. The tests were performed in nickel crucibles. No corrosion products were identified at the surfaces of the Mo samples (only NaO_2). The W samples formed Na_3WO_4 with oxygenated liquid sodium [71]. The corrosion of Mo was also studied in liquid sodium doped with charcoal, doped with titanium carbide, or with a stainless steel tab inserted at 600°C for 384 h.

In the presence of carbon in sodium, Mo_2C was observed to form. The amount of Mo_2C was a function of the amount of carbon available in the source (stainless steel or charcoal) [71]. Similar to other elements, the exposure of vanadium in oxygen-saturated sodium between 250 and 550°C led to the formation of Na_4VO_4 [85].

Contrary to all of the other pure elements (Cr, Fe, Ta, Ti, Zr, W) studied, the corrosion of Mo was not oxygen dependent. However, the formation of Mo_2C in the presence of carbon in sodium might alter its properties if it were used as a coating in SFRs.

Conclusions:

- Interaction between pure elements and sodium oxygen contents for up to 1,000 h and for temperatures between 400 and 650°C were studied (summarized previously in Figure 4). The compounds formed between pure elements and the sodium saturated with oxygen were identified and were found to be mostly oxides.

4.3 CORROSION OF STRUCTURAL MATERIALS IN STATIC AND FLOWING LIQUID SODIUM

As mentioned in section 3.3.1, dissolution of elements occurs when the chemical potential of element *i* in the alloy is higher than the chemical potential of the same element in the liquid sodium. In this section, the corrosion behavior of structural materials in static and flowing liquid sodium will be summarized. Since highly alloyed steels and nickel-based alloys have not been widely used in SFRs the focus will be mainly on conventional structural steels such as American Iron and Steel Institute (AISI) type 316 stainless steel or FM Grade 91 in static (reactor or capsule) or flowing sodium (TCL) experiments.

4.3.1 Corrosion of austenitic steels in static liquid sodium

For austenitic and ferritic steels, when the level of oxygen dissolved in liquid sodium is controlled under 10 ppm, two phenomena were observed during for the exposure of materials in liquid sodium. The first step was defined as a transient state which corresponded to the dissolution of the native oxide layers present on the surface of the samples. This step was observed to last for less than 24 h when the temperature was lower than 370°C and for a few hours above 550°C [86]. The second step, dissolution, was divided into two periods. The first period, was observed to last from several weeks at 600°C to about 300 h at 700°C and corresponded to the preferential dissolution of Ni, Cr, C, Si, and Mn [43]; sometimes, less soluble Mo and Fe were observed to increase at the metal surface [48]. Some authors related the Mo enrichment at the surface of the specimens to the formation of Fe_7Mo_6, Fe_4Mo_2C, or M_6C (with M as Cr, Mn, Fe, Ni or Mo) [42, 44, 45, 52]. For the austenitic steels, the chromium and nickel losses in the austenite matrix led to the transformation of the austenite (FCC structure) into ferrite (BCC structure) [43] and to the precipitation of sigma phase [52]. These processes occurred in the grains near the surface of the specimen and at greater depths at the grain boundaries, as austenite is not stable below ~8% nickel and ~15% chromium. The formation of a ferrite layer is illustrated for type 316LN steels exposed in liquid sodium at 550°C in Figure 7 from a secondary electron image and XRD measurements.

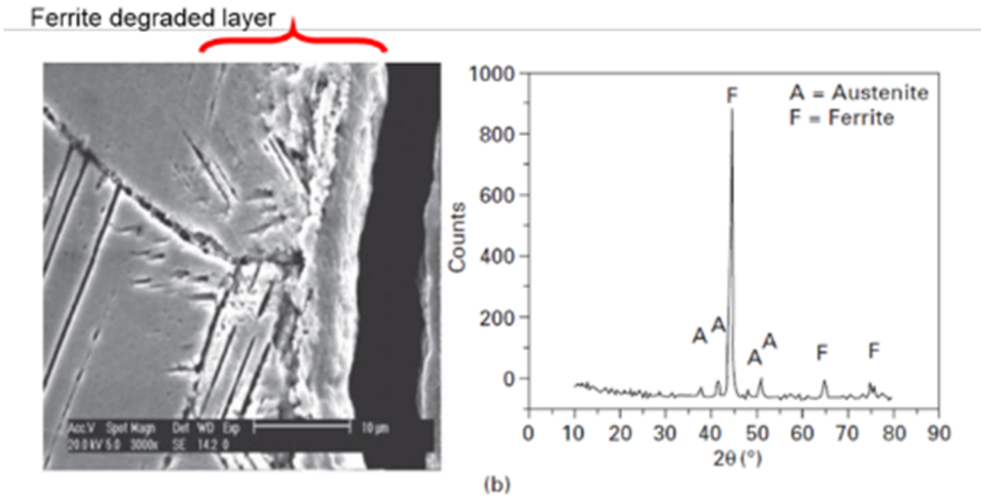

Figure 7. Scanning electron microscope micrograph of 316LN stainless steel exposed to liquid sodium at 550 °C, along with XRD diffractogram indicating the presence of ferrite on the surface of the steel (from [14]).

The second period, after the selective dissolution of constitutive elements of the steels, was a steady state corrosion in liquid sodium which is limited by the formation of the ferrite layer. During this period, the corrosion rate was observed to be constant. The growth of the formed ferrite layer was controlled by diffusion parameters [52]. According to Ganesan and Ganesan [52], diffusion data from diffusion couples should be considered, and a simple boundary condition can be used at the sodium\alloy interface. The two dissolution regimes are illustrated in Figure 8 for type 304 stainless steel exposed in high-velocity sodium at 760°C. Ganesan and Ganesan [52] observed both processes: selective leaching and steady state corrosion (growth of the surface ferritic layer) at T <500°C. At higher temperatures, the growth of the ferritic layer outweighed the selective leaching. They also observed less mass loss for cold-worked specimens compared with annealed ones, presumably as a result of increased diffusion rates in the cold-worked material.

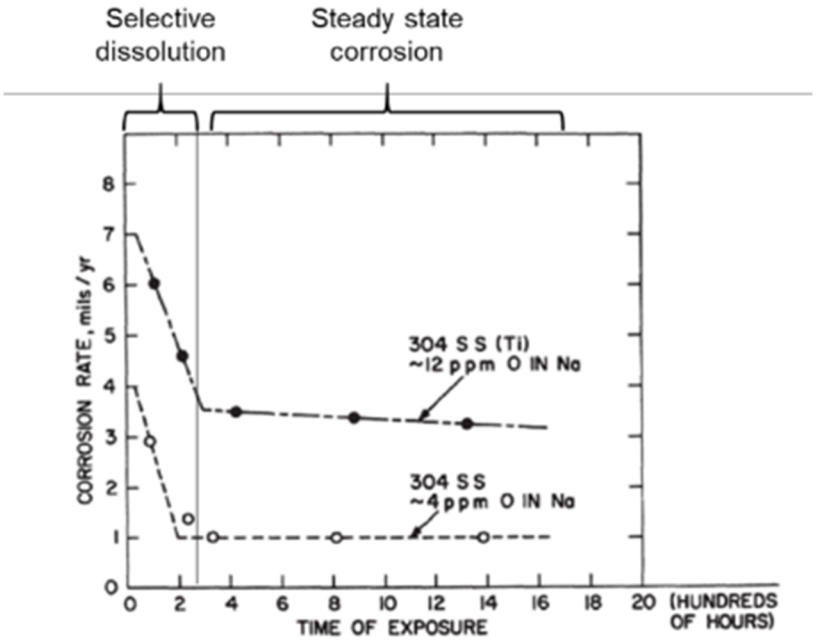

Figure 8. Effect of exposure time in high-velocity sodium at 760°C on the corrosion rate of 304 steel (from[43]).

4.3.2 Corrosion of nickel-based alloys and ODS alloys in static liquid sodium

For nickel-based alloys, the literature is very limited [43]. It was observed that nickel being the most soluble element it was controlling the corrosion in sodium containing oxygen levels lower than 10 ppm [76].

Literature data on the dissolution/corrosion of ODS FeCr and FeCrNi alloys, which are candidate materials for the fuel rod cladding, are scarce and were obtained using a 316SS TCL and oxygen-purified sodium [54].

Additional studies of ODS alloys without the influence of dissimilar material interactions are needed. To address this gap, the corrosion behavior of several ODS alloys was recently investigated at ORNL. The compositions of the investigated materials are reported in Table 2. The corrosion behavior of a common austenitic stainless steel (316H) was compared with the corrosion behavior of a commercial ferritic ODS FeCrAl alloy, Kanthal alloy APMT, a lower-chromium ferritic wrought FeCrAl alloy (C26M) and ODS FeCrAl, and ODS FeCr alloys, composition in Table 2 [87, 88]. The C26M material and the low-chromium ODS alloys were fabricated at ORNL. Specimens were SS-3 type tensile coupons (25.4 mm long, 0.76 × 5 mm gage) machined and polished to a 600-grit surface finish and cleaned in ethanol before exposure.

Three SS-3 specimens of each alloy were attached with Mo wires to the lids of capsules (25 mm outer diameter × 76 mm tall × 1 mm wall) made of low-carbon arc-cast (LCAC) Mo, as discussed earlier[72]). The capsules were filled with 25 g of commercial sodium (99.0 % purity, provided by Sigma Aldrich). Upon receipt, the sodium was covered with oxides. Another set of three SS-3 specimens of each material were inserted in similar Mo capsules filled with sodium, and a 25× 65 × 0.1 mm piece of Zr foil (99.5 wt. % purity provided by Sigma Aldrich) was added as an oxygen getter [84]. Each capsule was prepared in an argon-filled glove box with O_2 and H_2O impurity levels ≤1 ppm and was welded shut inside the glove

box using gas tungsten arc welding. The Mo capsules were then sealed in an electron beam–welded stainless steel capsule to prevent the primary capsule from oxidizing. A schematic representation of the capsules is presented in Figure 9, in which only one SS-3 specimen is shown for clarity. The capsules were then isothermally exposed in a box furnace in laboratory air for 1,000 h at 700°C. After cooling, the capsules were opened in the same glove box. For environmental, health, and safety concerns, the samples were cleaned sequentially using liquid ammonia, ethanol, and water to remove Na prior to handling and then weighed.

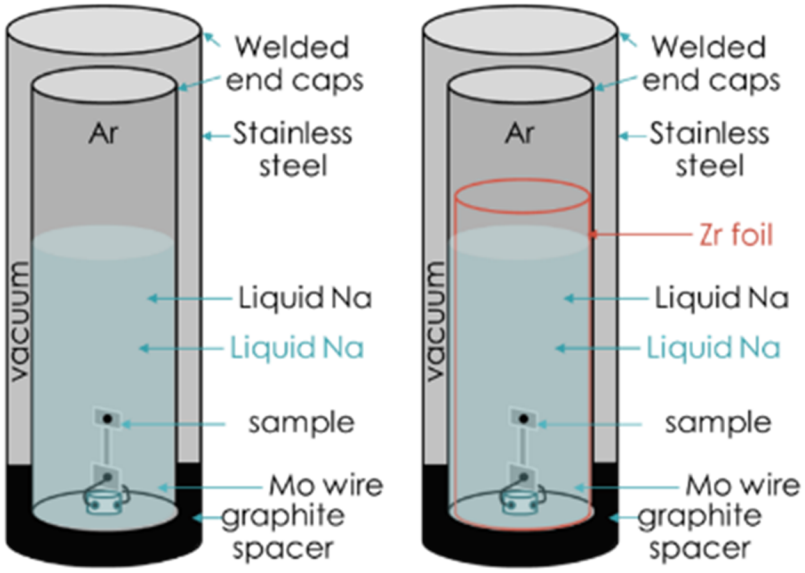

Figure 9. Schematic representation of the capsule containing sodium without Zr foil (left) and with added Zr foil (right).

The tensile specimens were tested at room temperature at a strain rate of 10^{-3} s^{-1}. Cross-sections of the exposed specimens were characterized using scanning electron microscopy (SEM), including energy x-ray spectroscopy (EDS) for elemental maps and profiles and electron backscatter diffraction. Etched cross-sections were also examined using an oxalic acid etchant (10g of $C_2H_2O_4$ in 100 mL water for about 2 s at 2 Vdc). In addition, specimens were examined by XRD.

After 1,000 h exposures at 700°C in sodium saturated with oxygen, the surfaces of the specimens were covered with a dark film that either spalled or dissolved in irregular patterns on the specimen surfaces during exposure and/or during the cleaning procedure (Figure 10 a, c, e, g, i), revealing the underlying corroded surfaces of the specimens. In sodium with Zr foil (i.e., low oxygen), the presence of the dark film was less noticeable (Figure 10 b, d, f, h, j).

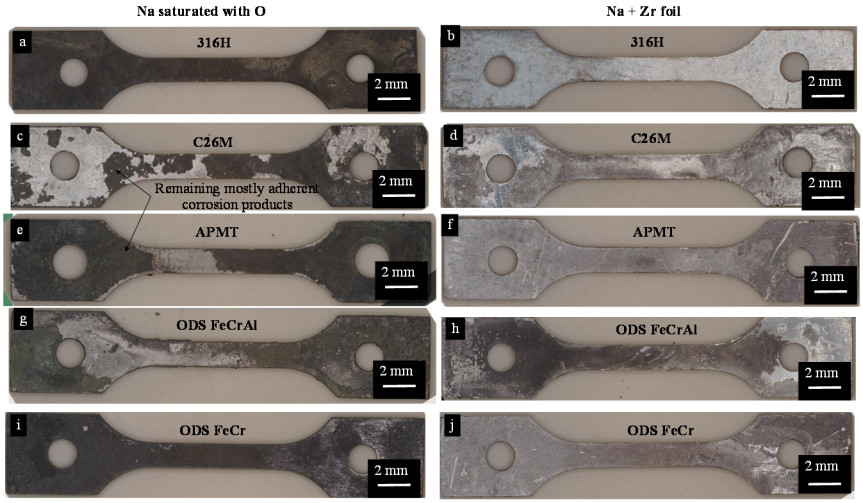

Figure 10. Optical images of (a, b) 316H, (c, d) C26M, (e, f), APMT, (g, h) ODS FeCrAl, and (i, j) ODS FeCr (Oak Ridge Fast Reactor Advanced Fuel Cladding) tensile specimens after 1,000 h exposure in static (a, c, e, g, i) sodium saturated with oxygen and (b, d, f, h, j) sodium with added Zr foil at 700°C.

Backscattered electron (BSE) images and EDS elemental maps of the 316H, APMT, and ODS FeCr specimens after 1,000 h of exposure in sodium saturated with oxygen at 700°C are shown in Figure 11 and Figure 12. After exposure, a Na- and Cr-rich oxide was formed on the surfaces of the three specimens, which was identified as $NaCr_2O_4$ by XRD measurements in agreement with previous literature findings on the surface of pure Cr and 316L(N) stainless steel after exposure to oxygen-rich liquid sodium [34, 35].

For the 316H specimen, a quite uniform $NaCr_2O_4$ surface layer was formed and penetrated along the grain boundaries of the alloy over about 30 ± 10 µm (Figure 11a,b and Figure 12a). The alignment of the Kα line of sodium with the Lα line of copper explains the sodium signal in the copper plating in Figure 12a. In addition, Mo enrichment was observed at the surface of the specimen (Figure 12a).

For the APMT specimen, a thinner, more uniform $NaCr_2O_4$ layer (1 ± 0.5 µm thick) formed above a Cr-depleted non-adherent layer (5 ± 1 µm thick) containing Cr- and Mo-rich and Fe-depleted precipitates (Figure 12b). Underneath these layers, an Al-rich oxide layer was identified. Finally, deeper in the alloy, Mo-, Zr-, Nb-, and Si-rich precipitates were observed (Figure 12b). These precipitates were previously found in APMT after annealing for 100 h in air at 500°C [89] and after 1,000 h of exposure in static and flowing Pb-Li at 500–650°C [90]. Thus, the precipitates are more relevant to the high-temperature thermal exposure and not related to the Na exposure.

For the ODS FeCr specimen, a non-uniform $NaCr_2O_4$ oxide scale was formed on the surface of the specimen (50 ± 5 µm thickness in Figure 11e, f). This oxide layer might have been dissolved or spalled, leaving a particularly damaged alloy surface. Underneath, a Cr- and Mo-rich phase was identified from EDS element maps (Figure 12c) as shown in Table 7 and the phase is clearly observed after etching (Figure 13). This phase was not present over (35±2 µm) underneath the oxide scale and then precipitated over 170±30 µm in the specimen (Figure 13).

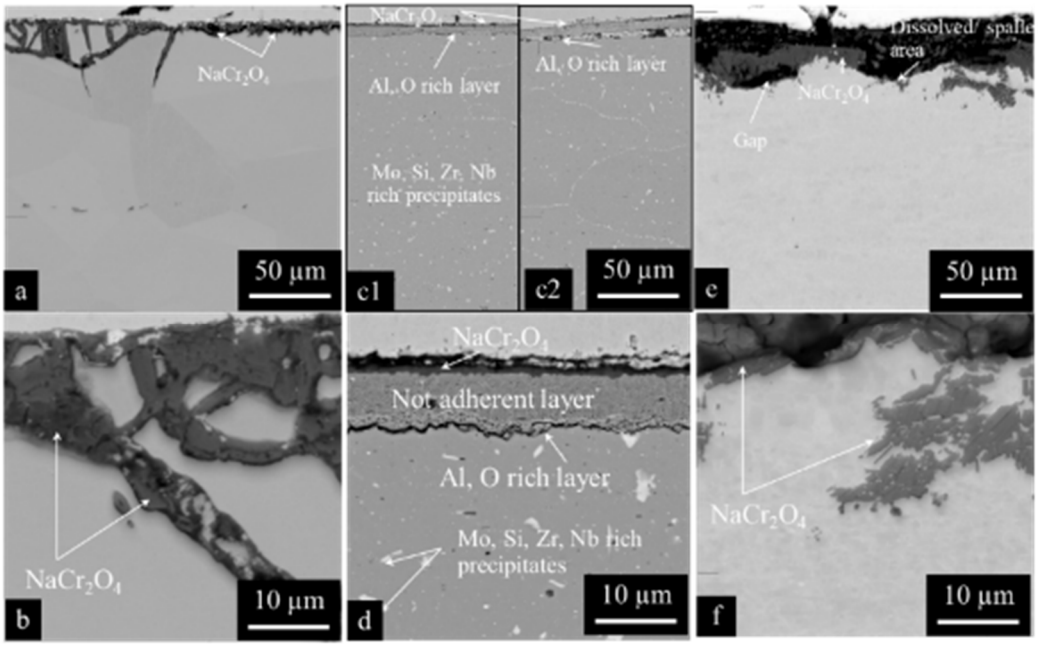

Figure 11. BSE images of (a, b) 316H, (c1, c2 , d) APMT, and (e, f) ODS FeCr after 1,000 h exposure in liquid sodium saturated with oxygen at 700°C.

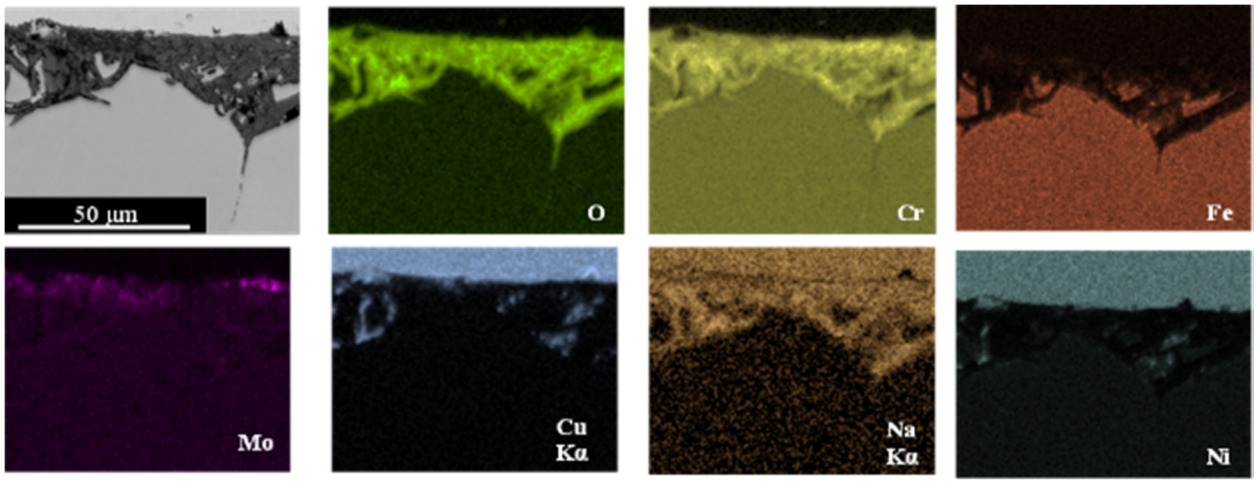
50 μm
O
Cr
Fe
Mo
Cu
Kα
Na
Kα
Ni

(a) 316H

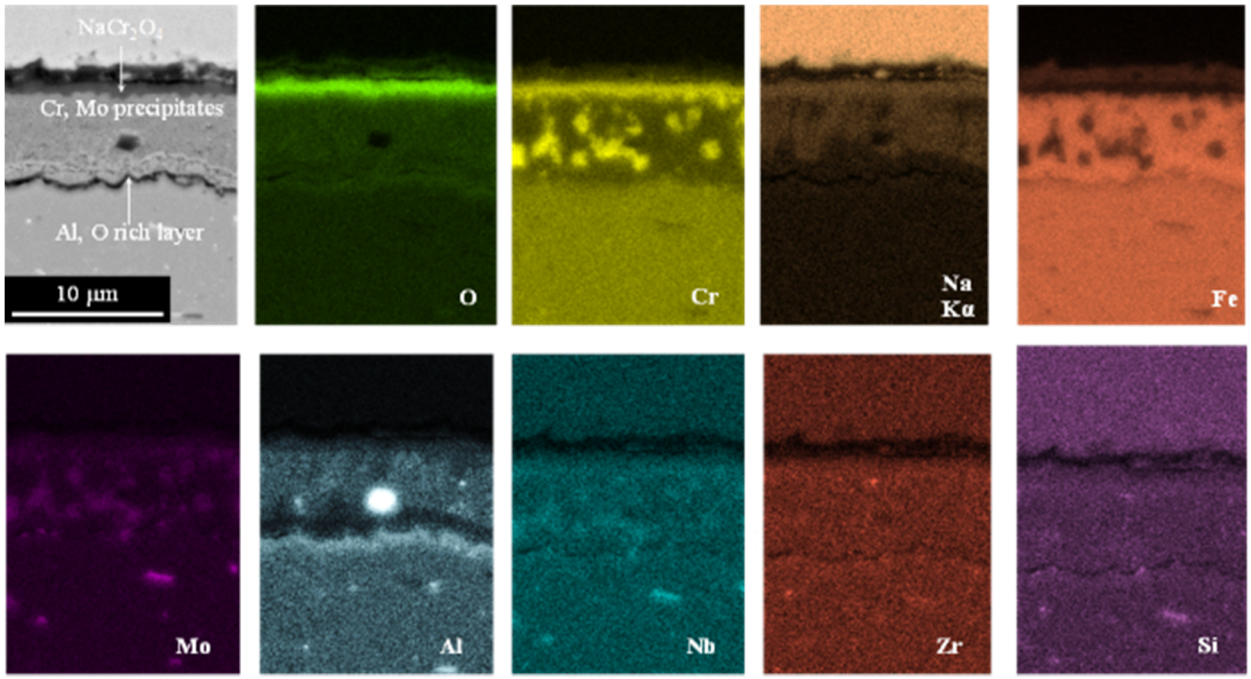
NaCr2O4
Cr, Mo precipitates
Al, O rich layer
10 μm
O
Cr
Na
Kα
Fe
Mo
Al
Nb
Zr
Si

(b) APMT

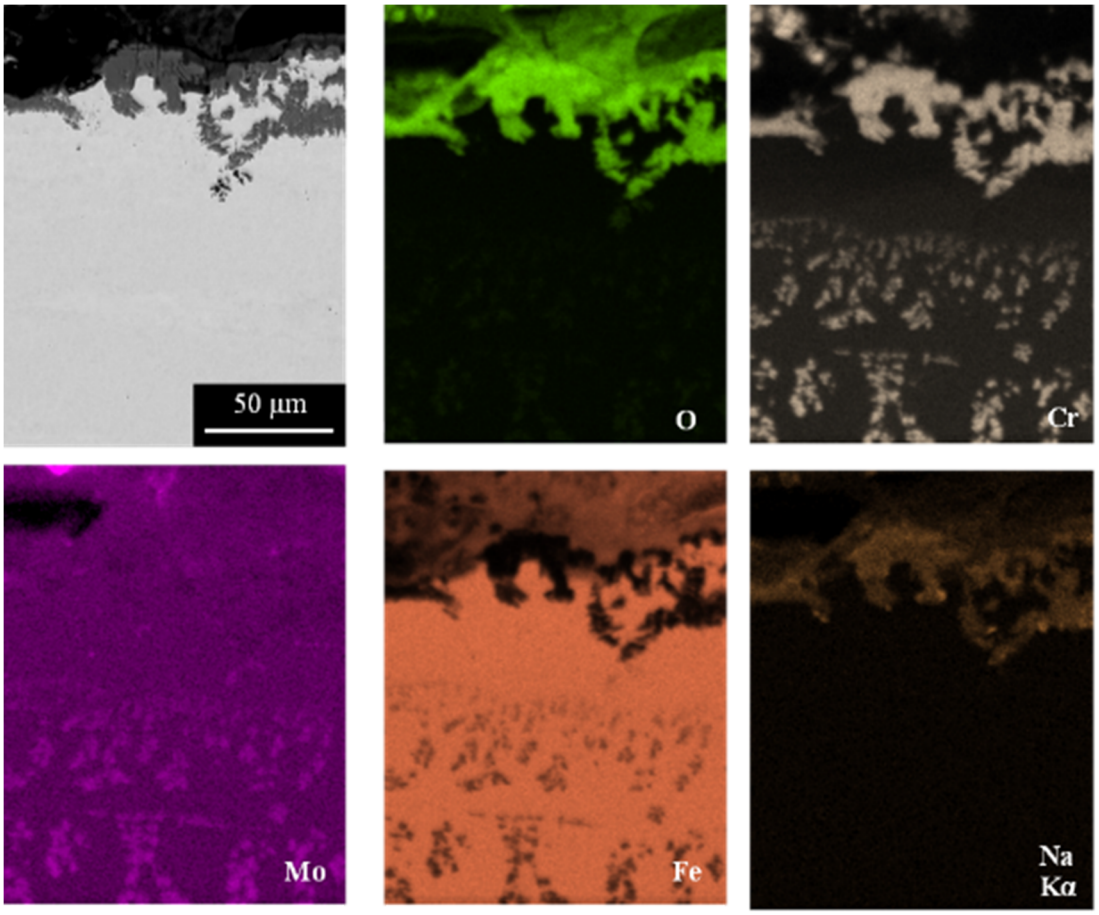

(c) ODS FeCr

Figure 12. EDS elemental maps of (a) 316H, (b) APMT, and (c) ODS FeCr after 1,000 h exposure in sodium saturated with oxygen at 700°C.

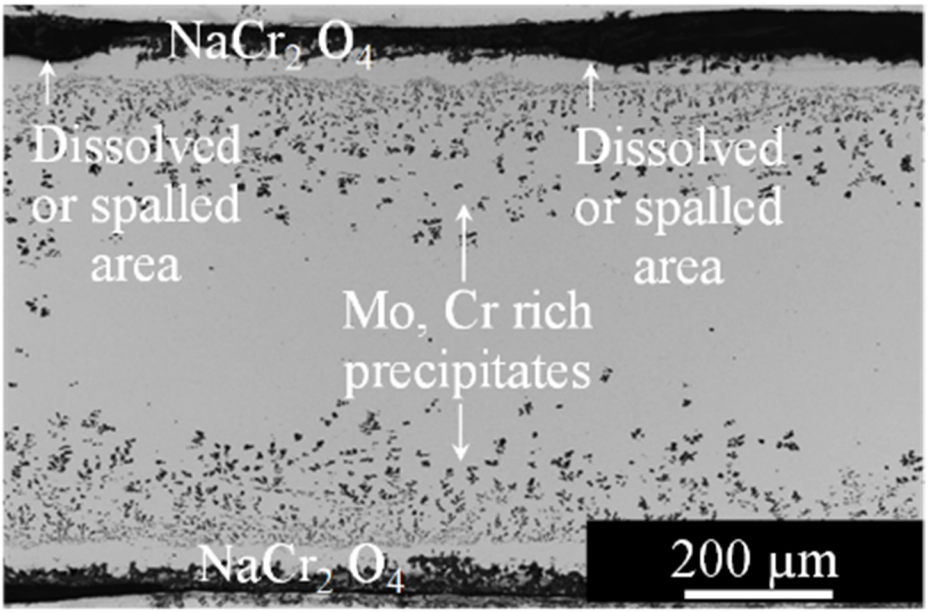

Figure 13. ODS FeCr specimen etched using oxalic acid solution after 1,000 h exposure in sodium saturated with oxygen at 700°C.

Table 7. EDS composition of Cr-, Mo-rich phase.

Element	Fe	Cr	Mo
wt. %	44.4	50.0	5.6

After exposure of the wrought FeCrAl C26M specimen in sodium saturated with oxygen, a non-uniform (curved) reaction front was observed with apparent porosity along the alloy grain boundaries (Figure 14a). One corner of the specimen was shown to be significantly depleted in Al, Cr, and Fe; rich in Mo and O; and notably deformed (Figure 15a and Figure 16). The surface of the specimen appeared rich in Al, Na, and O (Figure 17). Finally, etching of the specimen and EDS elemental maps revealed the presence of Cr, Mo, and O and Fe- and Al-depleted precipitates in the alloy (Figure 15b and Figure 17). In Figure 15b, a precipitation zone of 200±50 µm was measured away from the edges.

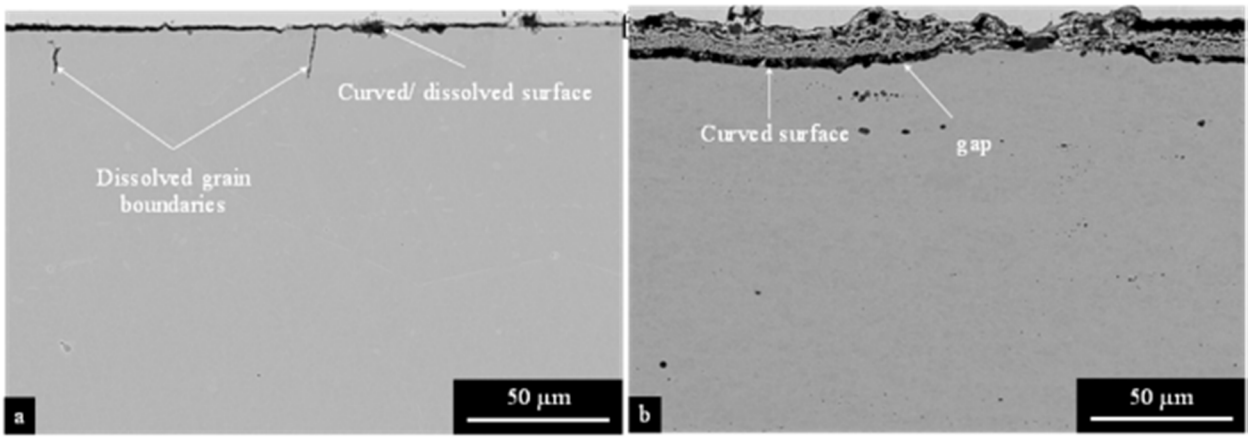

Figure 14. BSE images of (a) C26M (b) ODS FeCrAl after 1,000 h exposure in liquid sodium saturated with oxygen at 700 °C.

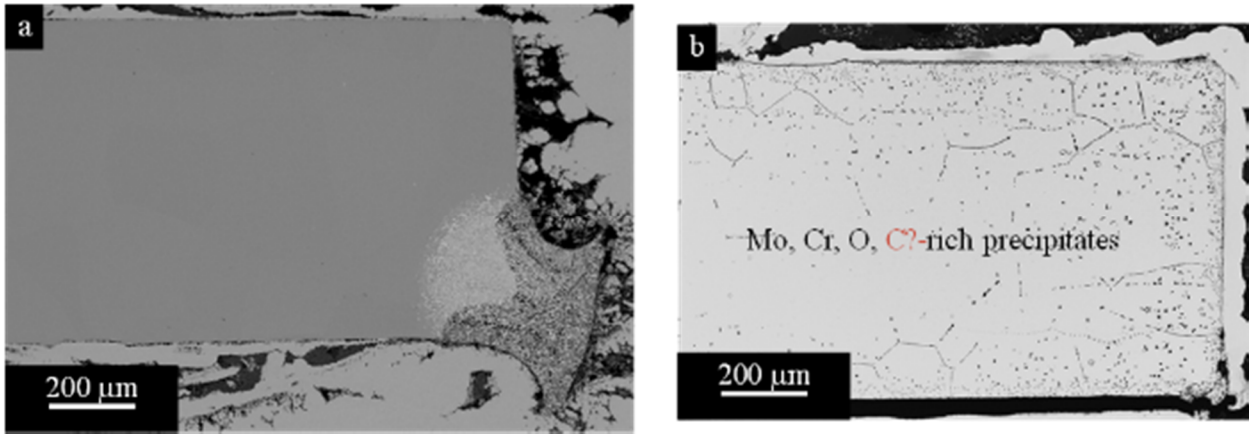

Figure 15. (a) BSE image and (b) etched optical image (oxalic acid) for C26M and 1,000 h exposure in liquid sodium saturated with oxygen at 700 °C.

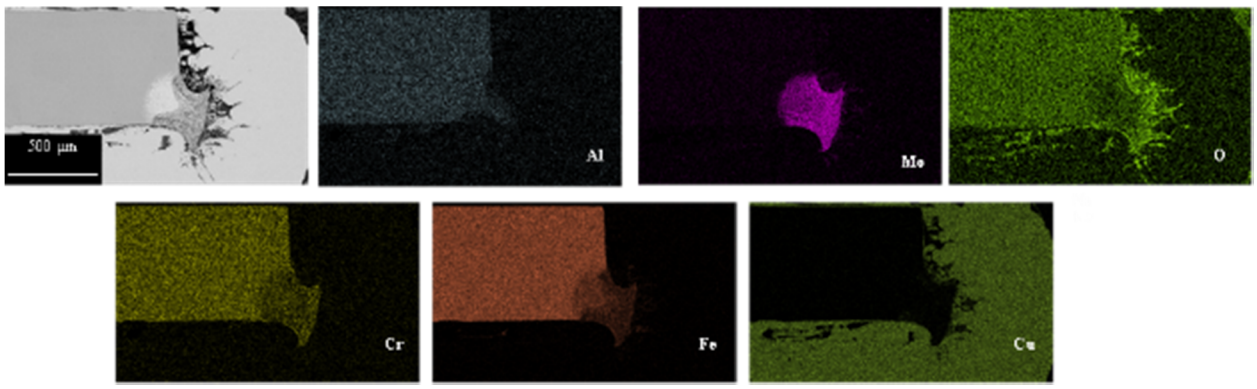

Figure 16. EDS elemental maps of corner of C26M specimen after 1,000 h exposure in sodium saturated with oxygen at 700 °C.

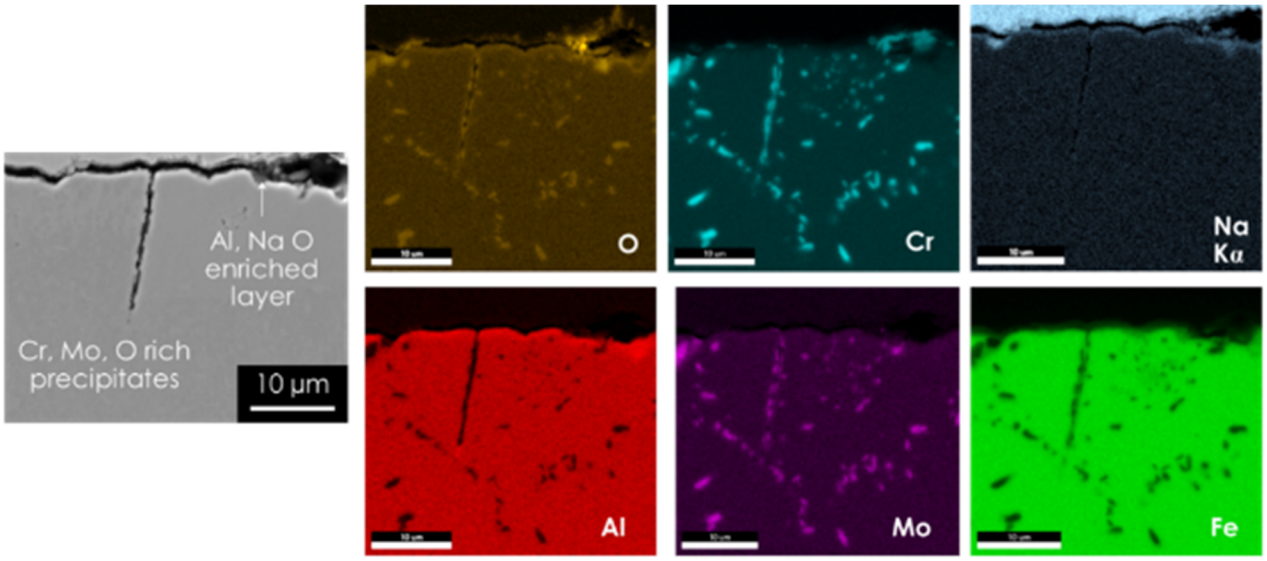

Figure 17. EDS elemental maps of C26M specimen after 1,000 h exposure in sodium saturated with oxygen at 700°C.

After exposure in sodium saturated with oxygen, the ODS FeCrAl specimen was covered with a non-adherent oxide layer (thickness of 6±2 µm) rich in Al and Na (Figure 18). Chromium- and O-rich precipitates were also identified, which were already present in the as-received material.

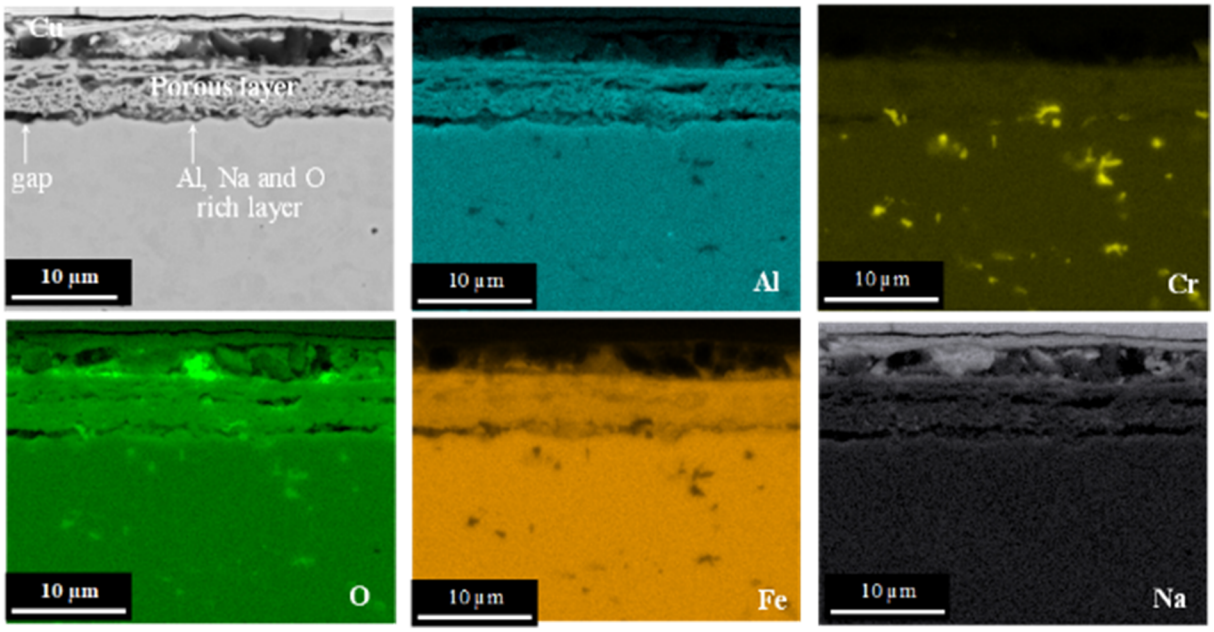

Figure 18. EDS elemental maps of ODS FeCrAl after 1,000 h exposure in sodium saturated with oxygen at 700°C.

Etched optical and non-etched BSE images of the specimens after 1,000 h exposures in sodium with added Zr foil are reported in Figure 19. No oxygen-rich corrosion product was identified on the surface of the 316H, APMT, and ODS FeCr specimens. For the 316H specimen, precipitation at grain boundaries of the alloy was revealed by etching (Figure 19a). Precipitates at grain boundaries were also observed after exposure in liquid sodium saturated with oxygen (not shown here). For the APMT specimen, a dense

precipitation zone (35±10 vol. % of precipitation) occurred in the grains of the alloy to a depth of 30±5 µm followed by a less dense precipitation zone (10±5 vol. % precipitates over 20±5 µm in Figure 19b). The precipitates were found to be C-, O-, Cr-, and Mo-rich and Al-depleted (Figure 20). A rough surface was also observed in Figure 21. In the ODS FeCr specimen, no precipitation was revealed either after etching or in the BSE images (Figure 19c, f), but significant surface roughening was observed (Figure 19c, f).

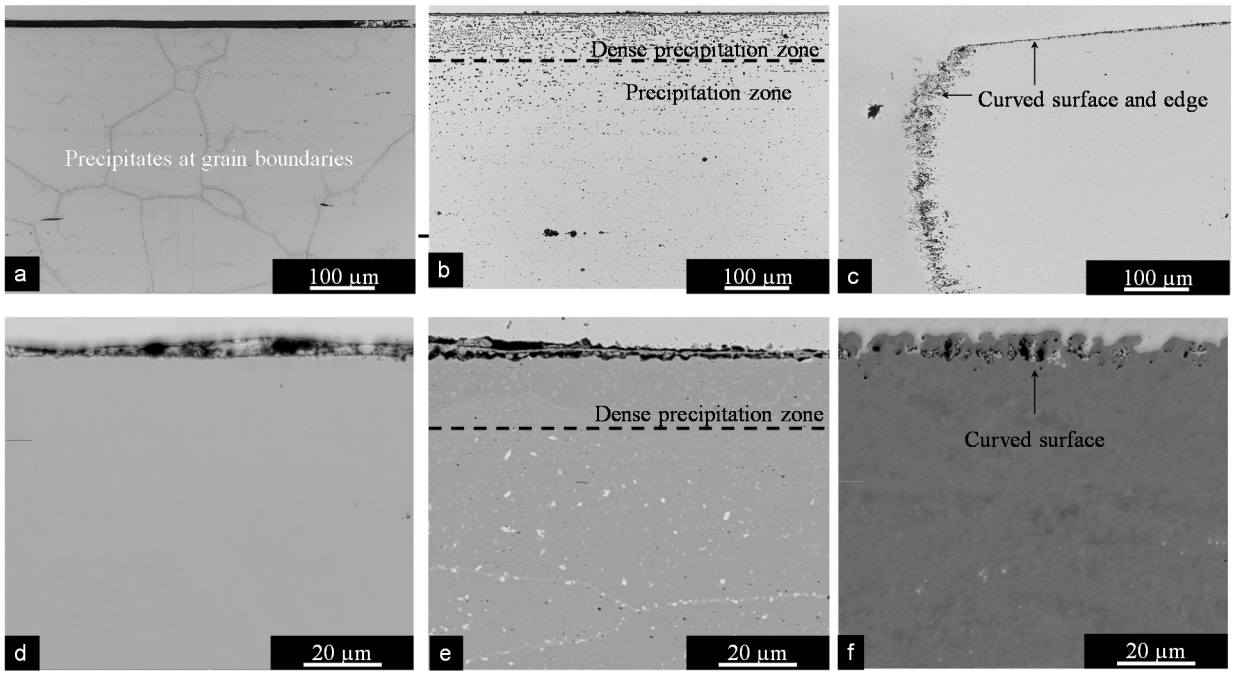

Figure 19. Etched optical (10 vol. % oxalic acid) and unetched BSE images of (a, d) 316H, (b, e) APMT, and (c, f) ODS FeCr after 1,000 h exposure in sodium with added Zr foil at 700°C.

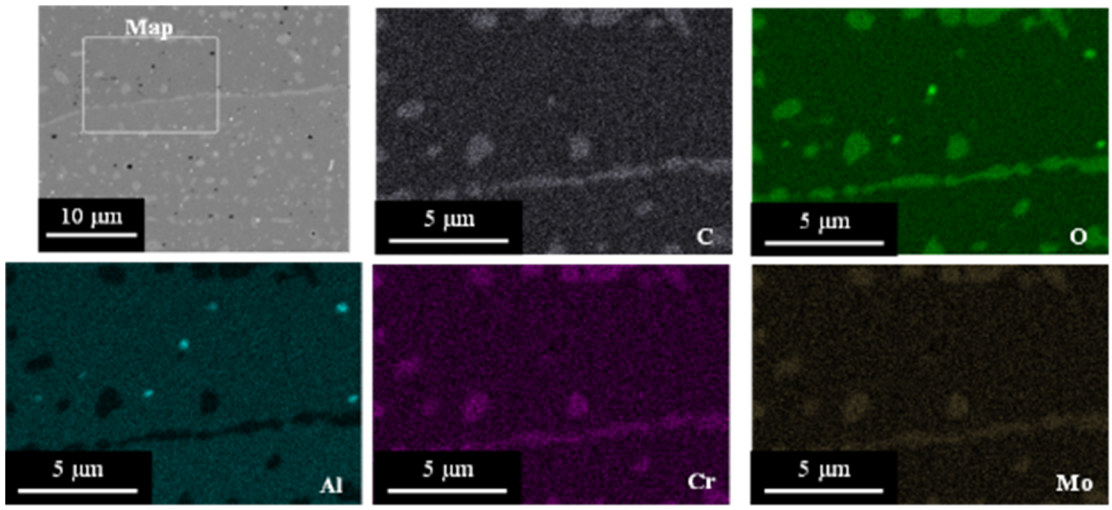

Figure 20. EDS elemental maps of precipitates near the surfaces in APMT specimen after 1,000 h exposure in sodium with added Zr foil at 700 °C.

In sodium with the Zr foil, similar Al- and Na-rich oxide layers were observed on the surface of the C26M specimen, along with the precipitation of Cr-, Mo-, and O-rich precipitates over 100±20 µm

(Figure 22 and after etching (not shown here). The ODS FeCrAl specimen presented a curved surface after exposure (Figure 19c, f) and no EDS elemental enrichments (not shown here).

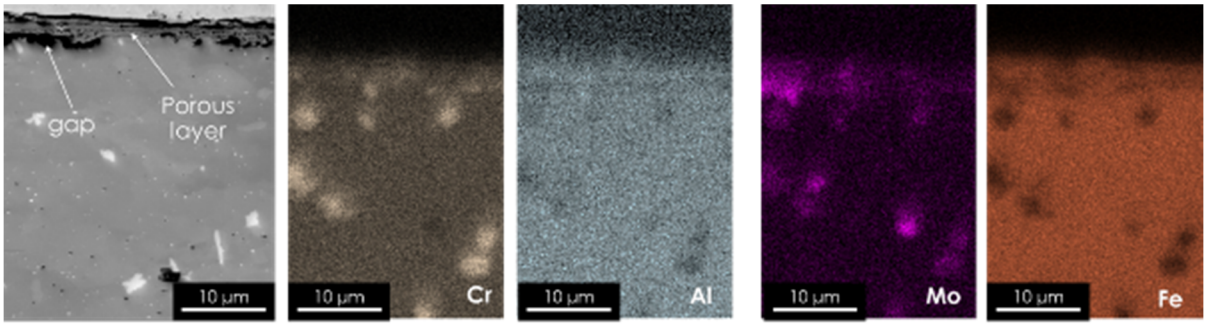

Figure 21. BSE images of APMT specimen after 1,000 h exposure in liquid sodium with added Zr foil at 700°C.

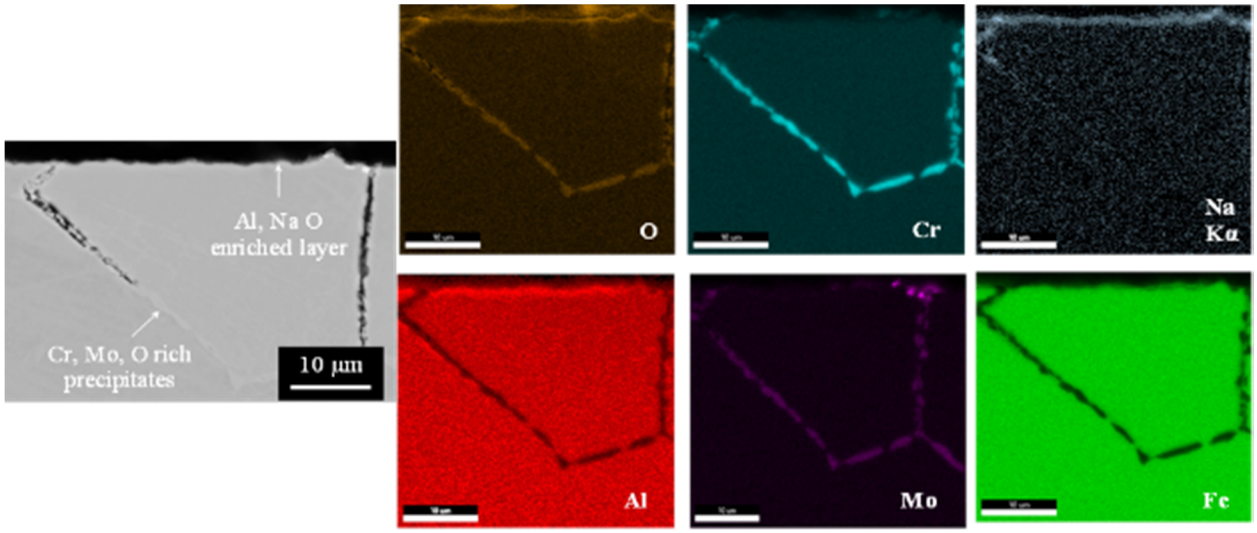

Figure 22. EDS elemental maps of C26M after 1,000 h exposure in liquid sodium with added Zr foil at 700°C.

EDS elemental profiles were measured in the underlying alloys to evaluate the extent of corrosion as a function of alloy composition and sodium oxygen content (i.e. sodium saturated with oxygen and sodium with added Zr foil). The chromium depletion profiles are reported in Figure 23 in sodium saturated with oxygen (closed symbols) and sodium with added Zr foil (open symbols) after 1,000 h of exposure at 700°C. Consistent with the formation of the observed $NaCr_2O_4$ surface reaction product, the alloys were depleted in chromium, as chromium diffused out of the alloy to form the reaction product. In contrast, only limited chromium depletion was observed for the 316H specimen in sodium both with and without the Zr foil (Figure 23a; less than 1 µm depletion in Figure 23a). A wide chromium depletion profile was measured for the ODS FeCr specimen with a chromium level under 12 wt. % over 200 µm in sodium saturated with oxygen because of the faster Cr diffusion in this BCC alloy. The thickness of the chromium-depleted zone corresponded to the thickness of the precipitation zone revealed after etching of the ODS FeCr specimen after 1,000 h exposure in sodium saturated with oxygen (see Figure 13). However, in sodium with added Zr foil, very limited chromium depletion was measured (over 5 µm in Figure 23a) when the formation of $NaCr_2O_4$ was limited.

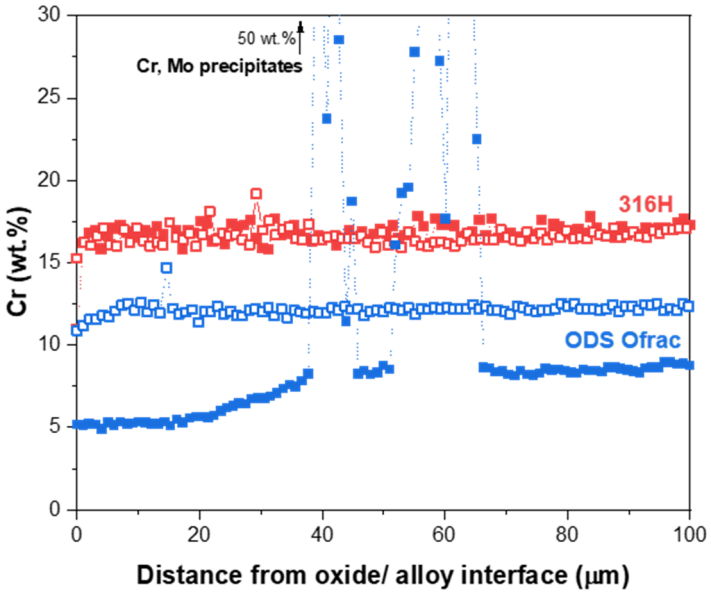

(a)

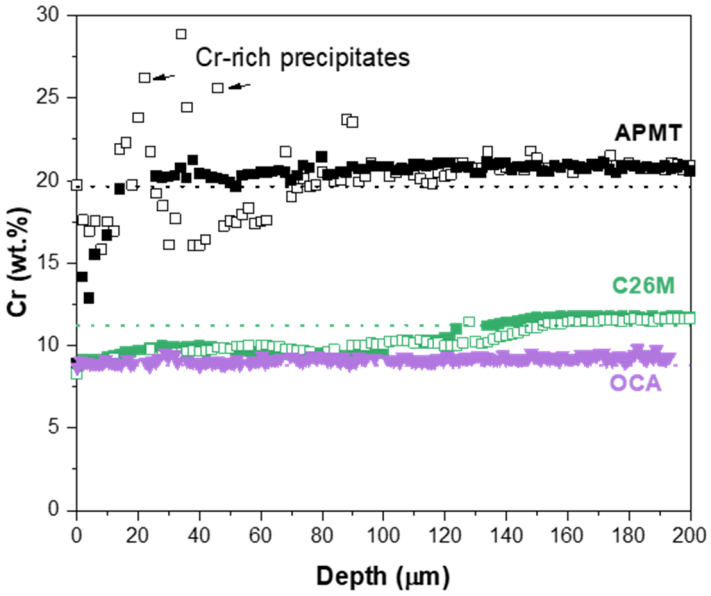

(b)

Figure 23. EDS chromium line profiles in the underlying (a) 316H and ODS FeCr (OFRAC) alloys and (b) APMT, C26M, and OCA after 1,000 h exposure in (closed symbols) sodium saturated with oxygen and (open symbols) sodium with added Zr foil at 700°C.

For the APMT specimen, chromium depletion was larger than for the 316H specimen measured over 10±3 μm (Figure 23b), with the Cr concentration being 12±3 wt. % near the surface compared to ~21% in the bulk alloy. The thickness of this zone corresponded to the thickness of the Cr-depleted zone identified from the EDS elemental maps in Figure 12b. In sodium with added Zr foil, the Cr depletion was measured at over 80 μm. The Cr concentration in this zone was measured at 17±2 wt. % with local Cr enrichments associated with the presence of Cr-rich precipitates (Figure 20). The thickness of this Cr-

depleted zone corresponded to the thickness of the precipitation zone revealed after etching the APMT specimen exposed to sodium with Zr foil (Figure 19b).

In the C26M specimen (Figure 23b), the chromium concentration was measured at 9±1 wt. % over 125 µm in the alloy in both environments. The thickness of this Cr-depleted zone corresponded to the thickness of the precipitation zone revealed after post-exposure etching for both environments (Figure 15b).

Aluminum profiles were also measured in the aluminum-containing alloys (Figure 24). Similar profiles were measured, in both environments, for the C26M and ODS FeCrAl (OCA) specimens over 40 and 25 µm depths, respectively. The aluminum concentration at the interface was 5±0.5 wt. %. For the APMT specimen, aluminum depletion was measured over a 30 µm depth, and lower aluminum concentrations were found in the depleted zone in sodium saturated with oxygen (1±0.5 wt. % at the interface) than in sodium with added Zr foil (3.5±0.5 wt. % at the interface).

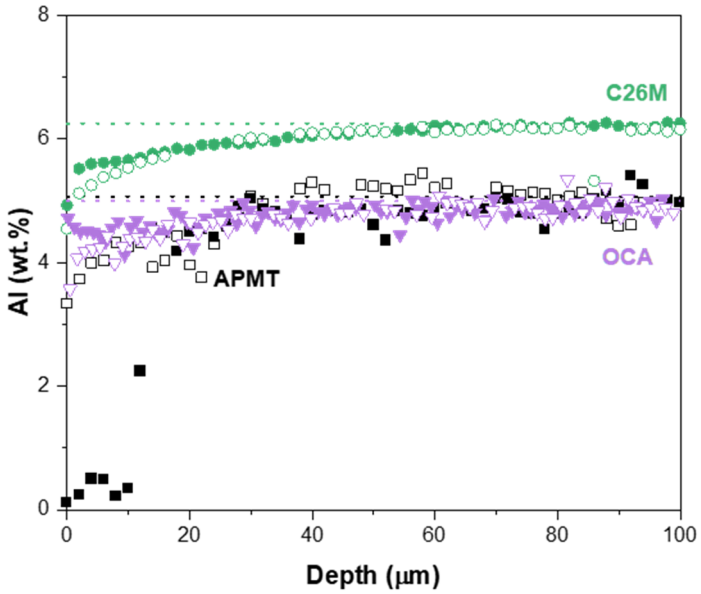

Figure 24. EDS aluminum profiles in the underlying APMT, C26M, and ODS FeCrAl (OCA) specimens after 1,000 h exposure in (closed symbols) sodium saturated with oxygen and (open symbols) sodium with added Zr foil at 700°C.

The room temperature tensile properties (ultimate tensile strength, or UTS, and fracture elongation (ε) of specimens before (single value) and after the 700°C exposures in sodium with and without Zr foil are reported in Table 8 and Table 9. Three tensile specimens per alloy were tested after exposure.

In liquid sodium saturated with oxygen, for the 316H and ODS FeCr specimens, a ~12% reduction in UTS and a 40-53% reduction in fracture elongation were measured after exposure (Table 8). For the APMT, C26M, and ODS FeCrAl specimens, quite stable or slight reductions in UTS and fracture elongation (less than 10% in Table 8) were reported after exposure.

Table 8. UTS and fracture elongation (ε) of specimens before and after 1,000 h exposure in liquid sodium saturated with oxygen at 700°C.

Specimens / Mechanical properties	316H	ODS FeCr	APMT	C26M	ODS FeCrAl
UTS – before exposure (MPa)	611	1,198	680	598	963
Sodium saturated with oxygen *UTS – after exposure (MPa)*	535±6 ↓12±1 %	1,059±12 ↓12±1 %	669±40 →stable	602±27 →stable	913±14 ↓5±1 %
ε – before exposure (%)	76	9.3	10	17.9	15
Sodium saturated with oxygen *ε at UTS– after exposure (%)*	36±1 ↓53±2 %	5.5±0.3 ↓40±3 %	12±4 →stable	16±1 ↓9±2 %	14±1 ↓7±3 %

Table 9. UTS and fracture elongation (ε) of specimens before and after 1,000 h exposure in liquid sodium with added Zr foil at 700°C.

Specimens / Mechanical properties	316H	ODS FeCr	APMT	C26M	ODS FeCrAl
UTS – before exposure (MPa)	611	1,198	680	598	963
Sodium with added Zr foil *UTS – after exposure (MPa)*	646±30 → stable	1,221±30 →stable	721±26 ↑6±4 %	573±47 →stable	936±6 ↓3±1 %
ε – before exposure (%)	76	9.3	10	17.9	15
Sodium with added Zr foil *ε at UTS – after exposure (%)*	52±2 ↓31±3 %	10±2 →stable	13±1 ↑24±10 %	11±4 ↓40 ±1 %	14±1 ↓10±5 %

In liquid sodium with added Zr foil, the UTS was slightly increased with respect to the unexposed specimens for the 316H and ODS FeCr and slightly decreased for the ODS FeCrAl specimens (Table 9). However, the fracture elongation was significantly decreased for the 316H and C26M specimens (31% and 40%, respectively, in Table 9) and almost unchanged for the ODS FeCrAl specimen (Table 9). Only the APMT specimen presented stable mechanical properties after exposure with respect to the unexposed specimen (Table 9).

4.3.3 Corrosion of ceramics in liquid sodium

The corrosion behavior of sintered, chemical vapor deposition, and single-crystal ceramics in liquid sodium was also studied after 1,000 and 4,000 h of exposure at 550 and 650°C in sodium containing 1 ppm of oxygen [91]. The tested ceramics are reported in Table 10.

Table 10. Tested ceramics from Kano et al. [91].

Sintered			
Existing	**Advanced**	**Chemical vapor deposition**	**Single-crystal**
Al_2O_3 ZrO_2	Al_2O_3		Al_2O_3 ZrO_2
MgO			MgO
Y_2O_3			
CaO			
$MgAl_2O_4$			$MgAl_2O_4$
$Y_3Al_5O_{12}$			$Y_3Al_5O_{12}$
SiC		SiC	
TiC		TiC	TiC
Si_3N_4	Si_3N_4		
AlN			
BN		BN	
SiAlON AlON			

It was observed that grain boundary attack was the dominant corrosion process for these ceramics and improvement of their corrosion resistance to sodium was needed if they were to be used in SFRs. Only this one study was found in the literature suggesting that more work may be needed, particularly for ceramics in contact with convention structural alloys in flowing sodium, where dissimilar material interactions may occur.

Conclusions:

- Many studies are specific to one material (Section 4.3). Additional studies are needed across a range of alloy classes (austenitic, ferritic, FM), composition (Ni-based, Ni-Cr-Fe based..), microstructures (e.g., annealed, cold-worked, varied grain sizes), and different conditions (static sodium, flowing sodium, carbon activity in sodium, sodium velocity, temperature gradient).

- ODS alloys can be very resistant to radiation damage and so are attractive for SFR fuel cladding applications. However, rather limited information has been reported regarding the sodium compatibility of these alloys, including FeCr and FeCrAl variants such as those developed for accident-tolerant LWR [87, 92, 93] (Section 4.3.2).

- Additional studies are needed to investigate chemical and microstructural changes of pure, binary, ternary and quaternary alloys after exposure to purified and unpurified liquid sodium over a wide range of conditions (static sodium, flowing sodium, carbon activity in sodium, sodium velocity, sodium temperature). These studies would provide necessary information toward the understanding of the corrosion of multi-components alloys in oxygen-purified liquid sodium and liquid sodium saturated with non-metallic impurities such as oxygen or carbon

4.3.4 Influence of sodium flow velocity

In the initial stages of flowing sodium experiments, the rate of metal loss was observed to increase with sodium velocity for turbulent or laminar flow. Then, when a critical velocity was reached, the dissolution of materials in liquid sodium was independent of the flow velocity of sodium (around 6 m/s). This effect was demonstrated by Thorley et al. in 1967 [94]. They measured the rate of 316 stainless steel metal loss

in stainless steel loops as a function of the nominal velocity, oxygen content in sodium, and temperature. The results are reported in Figure 25.

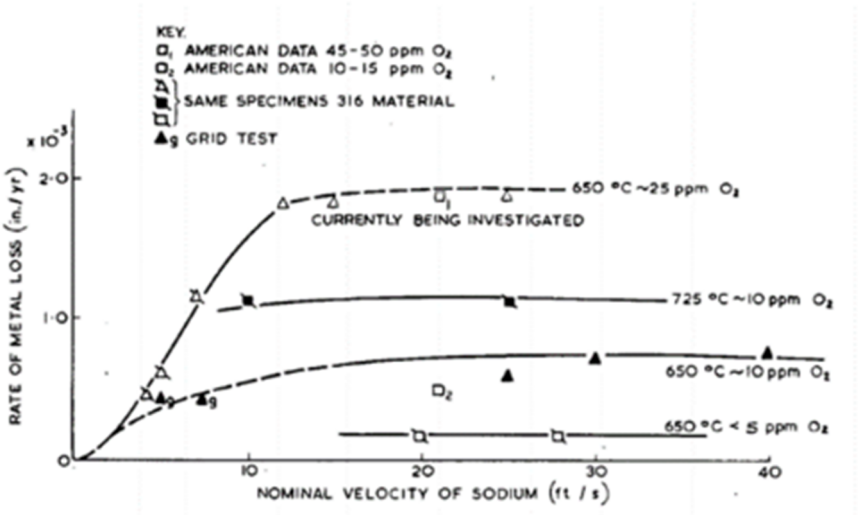

Figure 25. Effect of velocity on the dissolution of 316 stainless steel in a stainless steel sodium loop at 650°C and 725°C with less than 5, 10, and 25 ppm of oxygen [94].

4.3.5 Influence of oxygen and temperature

The corrosion rates of materials exposed in liquid sodium are strongly dependent on the oxygen content [47]. For example, at 650°C, for 316L stainless steel, Thorley et al. [94] observed that the corrosion rate was reduced by a factor of two when the oxygen content in sodium was reduced from 25 ppm to 10 ppm in sodium. The results are reported in Figure 26.

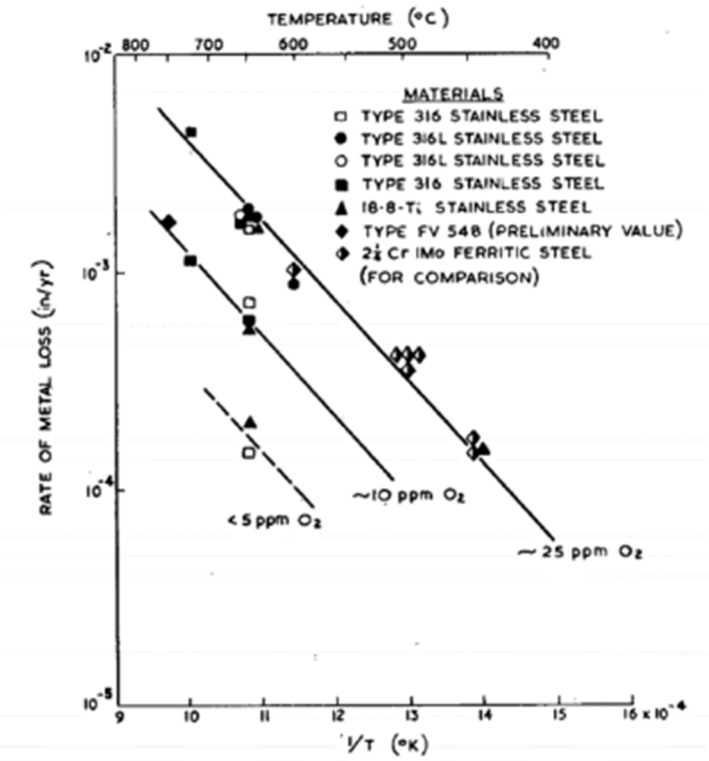

Figure 26. Effect of oxygen content in sodium on the rates of metal loss of different materials [94].

When the concentration of oxygen in sodium is higher than 10 ppm, the transient states of dissolution (wetting and selective leaching of elements) change. The transient dissolution step will be the formation of the most stable sodium ternary oxide with favorable kinetics. Different ternary oxides can be formed according to the stability of the oxides of the alloying elements (presented in Table 6) and their kinetics. These ternary oxides could be protective (i.e., inhibit the liquid-metal reaction) if the oxide formed is continuous and thus can limit further dissolution. Otherwise, if the product is unstable in sodium, it can increase the dissolution rate of the element that formed the oxide.

For iron-based alloys, when the level of oxygen dissolved in liquid sodium was above 10 ppm, in the initial stages, oxidation of the specimens was observed (formation of $NaCrO_2$ [42] or the most stable oxide in sodium from Table 6). In a TCL, the initially formed oxide can be removed and transported from hotter regions to colder regions. The $NaCrO_2$ is unstable in sodium and is dissolved. Then, steady state corrosion takes place (with a constant dissolution rate).

In the early stages, the corrosion behavior of Ni-based alloys was little affected by the sodium oxygen concentration up to 500 ppm [94]. This can be explained by the fact that, in these alloys, ternary oxides formed at equilibrium are less likely to form than in iron-based alloys when the level of oxygen in sodium is low.

Conclusions:
• Studies conducted with varied levels of oxygen suggest that to reduce oxidation and dissolution and maximize the lifetime of structural materials (mainly stainless steels) in SFRs, including increasing

their safety, the oxygen level in sodium should be monitored and controlled below 1 ppm (Sections 3.2, 3.3.4, 4.3.1, 4.3.2, 4.3.5).

- More work is needed to understand if there is a critical O content that should be maintained during operation to minimize corrosion and maximize the corrosion lifetime for each class of structural alloys. Also, the effect of short-term disruptions in O content of sodium on compatibility has not been evaluated.

4.3.6 Influence of TCL or FCL on the corrosion behavior of materials in liquid sodium

The mass transfer under thermal gradients is represented in Figure 27. Usually, in hot zones, dissolution occurs because the chemical potential or the solubility of the studied element in the alloy is higher than its chemical potential in the liquid sodium. As the flowing liquid moves to the cold zone, solute deposition (precipitation) of the studied element can occur because the solubility of this element in the sodium decreases significantly and the liquid sodium can become oversaturated.

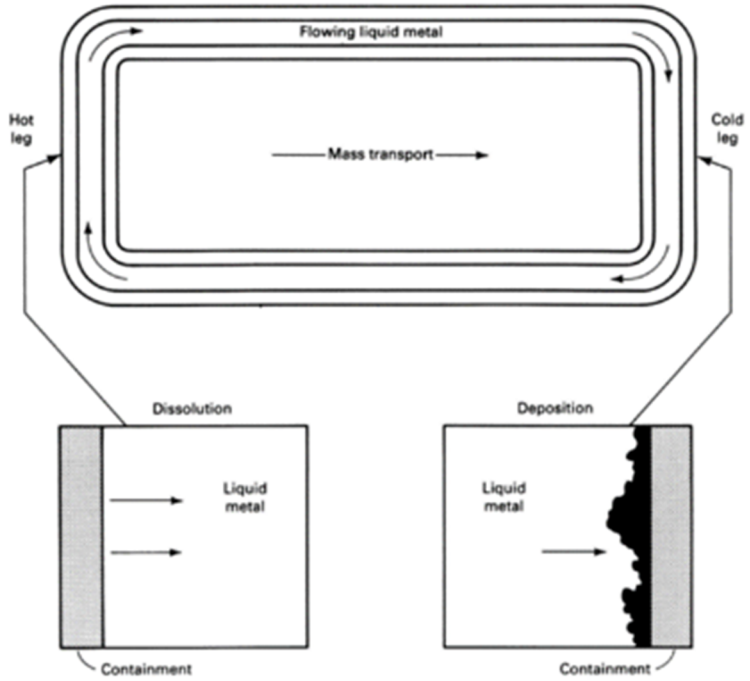

Figure 27. Schematic representation of a mass transfer phenomenon under thermal gradient in a circuit (from [39]).

In the case of dissolution of alloys (not pure metals) in liquid sodium, the dissolution rates and solubilities of multiple elements (*i, j, k*) must be taken into account in Eq (7). Assumptions must be made regarding the temperature, the dissolving elements in the liquid sodium, and the sodium chemistry (chemical potentials of compounds formed in sodium at equilibrium with the structural materials). Therefore, the usefulness of this equation is somewhat limited. A thermodynamic and kinetic approach must be applied.

The effect of system geometry is sometimes called a “downstream effect” or “mass transfer effect.” In a TCL, the chemical potentials of the corroding species (simplified as solubilities) vary along the sodium circuit because of the temperature variation. Consequently, the dissolution phenomenon is accentuated (evolution of the thickness of the ferrite layer). Most of the research studies were focused on corrosion

and mass transfer of austenitic and ferritic stainless steels in sodium loops [17, 45, 49, 54, 72, 79, 94-101]. The important factors to consider for the corrosion behavior of materials in liquid sodium are the effect of loop tubing composition and the presence of dissolved oxygen in the flowing sodium. In fact, as mentioned previously, the presence of oxygen will induce the formation of ternary oxides in sodium and thus will tend to enhance the dissolution of structural materials. Furthermore, the introduction of materials with dissimilar compositions (alloy studied versus loop materials) will result in different activity gradients and thus different mass transfers (compatibility issues). For example, if one alloy has a higher chromium or nickel activity, it will likely be selectively attacked; and the second alloy may show a particularly low reaction rate.

A few studies have been reported with a low oxygen level in the sodium (1–2 ppm) [49, 54, 97]. In those three studies, an FCL made of type 316 SS was filled with flowing sodium at velocities between 4 and 6 m/s^{-1} at 600 or 700°C. The researchers studied the corrosion behavior of 316 SS, solution-hardened 310, 330, Inconel 718, or ODS steels inserted in the loop (compositions in Table 2). Dissolution and carburization of the studied materials were observed in each case except the ODS alloys, in which deposition of nickel was observed [54]. In that case, nickel was dissolved from the 316 loop and diffused into the FeCr ODS steels. This phenomenon was induced by the nickel activity gradient in the loop created by the presence of dissimilar materials (ODS steel and 316). There is an active program at Argonne National Laboratory (ANL) studying the compatibility of Grade 91(G91) and Grade 92 (G92) FM steels in liquid sodium [81]. The corrosion and tensile behavior of G91 and G92 were studied in an austenitic stainless steel FCL containing about 20 kg of sodium with the oxygen level controlled below 1 ppm. The specimens were exposed for up to 20,000 h at 550, 600, and 650°C. At 500 and 600°C, liquid sodium exposure (at an oxygen level below 1 ppm) of G91 and G92 in an austenitic stainless steel loop was found to have an insignificant effect on the microstructures of the specimens (grain size, carbide size and fractions, laves phases) and was observed to degrade the tensile properties by less than 10%. However, at 650°C, drastic reductions of the tensile properties of the materials were observed (more than 50% reduction). This result was related to the thermal aging and decarburization of the specimens in liquid sodium [81].

Other studies were performed in the presence of 2–25 ppm of oxygen in sodium [45, 78, 79, 94-96, 98-104]. In addition to the formation of ternary oxides, some compatibility issues were reported. For example, Grade 22 ferritic steels (2.25Cr-1Mo) were investigated in a sodium loop made of a different material (mainly 316 or 304 austenitic steels) [94, 96]. In these studies, the decarburization of Grade 22 ferritic steels was observed. In other investigations, the sodium loop was bimetallic, made of Grade 91 and 316LN [94, 96, 100, 101, 104]. In those studies, carburization of both materials was observed, to a larger extent for the FM Grade 91 steel. In addition to the compatibility issues (introduction of dissimilar materials in a sodium loop), carburization and decarburization were shown to be a concern for the long-term mechanical properties of structural components in liquid sodium. It is unclear whether the carburization was induced by a chemical potential gradient created by the introduction of two materials in liquid sodium, or sodium is carburizing by nature. The following section explores this phenomenon.

More complex mass transfer models have been proposed in the literature [40, 105, 106]. Using mass and composition change as a function of the temperature, these models can provide kinetic data and identify the rate-controlling mechanism (e.g., surface reaction, liquid phase diffusion through the boundary layer, and solid-state diffusion in the alloy) of mass transport for a closed tubular liquid metal system. Limitations of such analyses apply when the solution rate constant, k_i, varies around the circuit, as well as the change of the controlling steps within the temperature range. For example, the surface reaction can be the rate-controlling step in one part of the circuit, whereas solid-state diffusion can be the rate-controlling step in another part. Furthermore, when different elements from the constitutive alloy of the loop are involved in the mass transfer, each element must be handled with its own set of thermodynamic and

kinetic parameters [40]. The ultimate goal is to develop corrosion lifetime models, which is extremely complex with flowing sodium in a temperature gradient.

Conclusions:
• TCL and FCL experiments incorporate many different variables in each experiment. More thorough investigations are needed in flowing sodium of integral effects of parameters such as temperature gradient, oxygen content, carbon content, velocity, and dissimilar materials. These fundamental studies would assist in developing more accurate and predictive corrosion models.

4.3.7 Corrosion lifetime models: Corrosion rates of austenitic steels in liquid sodium

Most of the corrosion studies in the literature were performed with dissolved oxygen and corrosion rate expressions were proposed. Several corrosion rate relationships for austenitic stainless steels are provided in the literature. According to Kolster et al. [45], the steady state corrosion of austenitic stainless steels in sodium containing up to 8 ppm oxygen, with a sodium velocity of 6 m/s^{-1}, was linearly dependent on the oxygen level (Eq. [8]).

$$I\ (mg.cm^{-2}.yr^{-1}) = K + C(O)\ , \qquad 8$$

where *O* is the oxygen content in sodium (in ppm), *K* is the rate constant for dissolution of metallic elements in sodium, and *C* is the rate constant for the reaction of metallic elements with oxygen. Values of *K* and *C* at 650 and 700°C were reported [45]. Equation (9) is the reported corrosion rate expression from Thorley and Tyzack [94] for the dissolution of 316L steel in the temperature range 450–725°C with higher oxygen levels in sodium (>25 ppm).

$$S\ (cm/s) = 2.3\ 10^{-6}\exp(-17500/RT)\ . \qquad 9$$

The latter equation was modified by Ganesan et al. [52] for austenitic stainless steels in static sodium. The expression is given in Eq. (10) considering the oxygen content in sodium.

$$\text{Log S(mil/year)} = 2.44 + 1.5\log(O/\text{ppm}) - 18000/(2.3RT(K))\ . \qquad 10$$

A more recent corrosion rate expression was proposed by Yoshida et al. [78] for the evolution of the degraded layer of 304 stainless steel used as piping in a sodium loop exposed for 10,000 h at 500, 550, and 600°C. In this study, the concentration of dissolved oxygen was less than 10 ppm. The three relations are given in Eq. (11).

$$\begin{aligned} &\text{At 600 °C, Y (microns)} = -112.5 + 32.5\log(t/h)\ . \\ &\text{At 550 °C, Y (microns)} = -97.1 + 25.8\log(t/h)\ . \qquad 11 \\ &\text{At 550 °C, Y (microns)} = -64.7 + 17.2\log(t/h)\ . \end{aligned}$$

It is important to mention that all these expressions were established for a specific material composition (304 or 316 stainless steel) and for a defined oxygen concentration range dissolved in sodium. These equations do not apply to ferritic steels or ODS (Fe-9Cr1Mo, 0.25Cr1Mo, FeCrAlY) alloys because the dissolution steps and kinetics are different. Being able to predict the corrosion rate for a wide range of chemical compositions would be very useful for future lifetime evaluations.

Conclusions:

- The previous corrosion models/rates were developed only for type 316 or 304 austenitic stainless steels in very specific experimental conditions. Each corrosion rate law is valid solely for the set of parameters presented in each study (e.g. temperature, sodium O content and alloy composition).
- The extent to which these laws can be extrapolated to longer duration or to different alloy and sodium chemistries were not studied. Therefore, the authors would recommend using these corrosion rate laws with precautions.

4.4 CORROSION BY CARBON, CARBURIZATION

Carbon transfer occurs between materials exposed in liquid sodium when the chemical potential of carbon in sodium is higher than in the studied steel. Previous studies confirmed that, along with the dissolution of structural materials into sodium, carburization can occur. The latter phenomenon has been well studied. The first studies about carbon transport in the sodium-steel system were performed at the Atomics International Division of North American Aviation [107], ANL and UKAEA [61, 108]; other studies followed [60, 62, 66, 109, 110]. More recently, for the development of the new SFR in India (PFBR), Japan (the liquid metal fast breeder reactor), and France (ASTRID), carburization in sodium loops was studied [28, 65, 79, 100, 101, 103, 104, 111].

4.4.1 Carburization in high carburizing sodium ($a_c = 1$)

The first studies were performed in severe carburizing conditions to understand the carburization mechanism, microstructure, and kinetics [61, 62, 107-109].

4.4.1.1 Microstructure and nature of the carbides

Anderson et al. [107] exposed type 304 and 316 austenitic SS in sodium saturated with carbon at 648°C for 5,300 h. Gwyther et al. [109] exposed types 316 and 316LN SS in carburizing sodium for 243 h at 643°C. Finally, Dickson et al. [62] exposed type 316 SS for 168 h at 600 C in sodium saturated with carbon. In the three studies, two different microstructures were observed after etching: a first zone called the “intragranular carburization zone” followed by a second zone called the “intergranular carburization zone.” Examples of the two microstructures are shown in Figure 28.

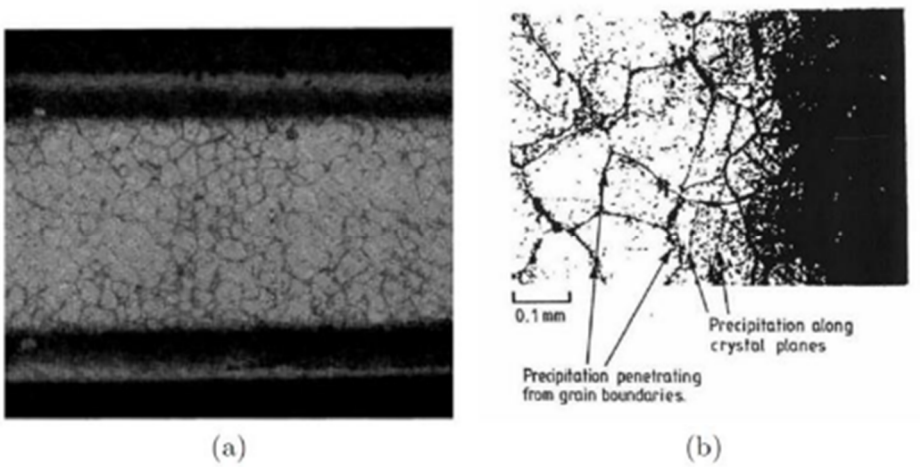

Figure 28. Microstructure of type 316 SS (a) 760 µm thickness after 243 h at 643°C in carburizing sodium [109]. (b) after 168 h exposure in carburizing sodium at 600°C [62].

The microstructures after carburization of other steel grades were recently studied. Two austenitic SS, 15Cr15Ni0.4Ti and 316L, and one FM steel, Grade 91, were exposed in liquid sodium for 500, 1000, 3000, and 5,000 h at 600°C in carburizing sodium (activity of carbon >1) [65]. As in the previous studies, two carburization zones were observed for the austenitic steels and evolved with exposure time. For the FM steel, only one carburization zone was observed (Figure 29).

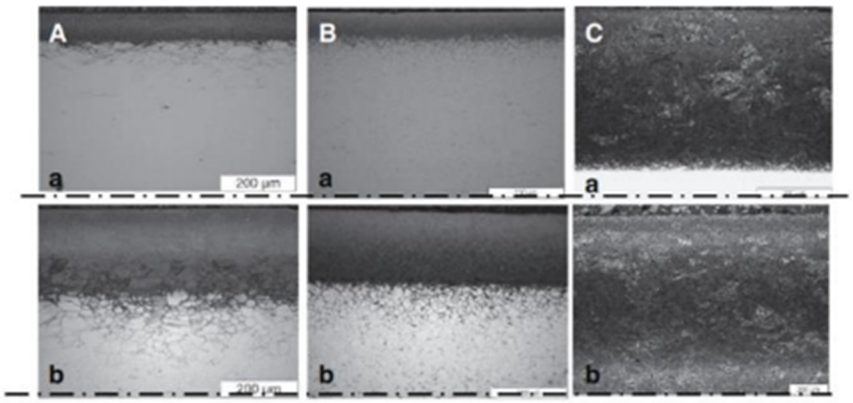

Figure 29. Microstructure of (A) 15Cr15Ni0.4Ti, (B) 316L, and (C) 9Cr1Mo steels after exposure for (a) 500 h and (b) 5,000 h at 600°C [65].

In all the studies, M_7C_3 and $M_{23}C_6$ carbides (with M = Fe, Cr, and Mo, mainly) were identified in austenitic stainless steels. In 9Cr-1Mo martensitic steels, only M_3C (M= Fe, Cr, and Mo, mainly) was characterized.

4.4.1.2 Carburization kinetics

The kinetics of carburization of materials exposed in liquid sodium was first studied by Natesan and Kassner [108] and Thorley and Hobdell [112]. The first group observed that the carburization kinetics of SS in sodium involved diffusion of carbon in austenite accompanied by partial carbide precipitation. As a consequence, the Wagner model for internal oxidation [113] would greatly underestimate the precipitated carburized zone. The carburization kinetics should be described considering the diffusion of carbon

coupled with rapid carbide precipitation, and equilibrium partitioning of carbon between the metal and precipitate phases [61, 65].

Initially in the literature [62, 107, 109, 114], the carburization kinetics were determined using the solution of Fick's second law (Eq. [12]) [115].

$$C(x,0) = C_0 \text{ x} > 0, \text{ t} = 0$$

$$C(0,t) = C_S \text{ x} = 0, \text{ t} > 0 \qquad 12$$

$$\frac{C(x,t) - C_0}{C_S - C_0} = erfc\left(\frac{x}{2\sqrt{D_{app}t}}\right),$$

where

- $C(x,t)$ is the carbon concentration (wt. % or at. %)
- C_S is the carbon concentration measured at the surface of the alloy when steady state is reached (wt. % or at. %)
- C_0 is the initial carbon concentration in the alloy (wt. % or at. %)
- x is the specimen thickness (cm)
- D_{app} is the apparent diffusion coefficient of carbon in the alloy (cm^2/s^{-1})
- t is the exposure time (s)

The apparent diffusion coefficient, D_{app}, is not the diffusion coefficient of carbon in the austenite or ferrite matrix. Instead, it is a fitting parameter used to evaluate the thickness of material affected by carburization (intragranular and intergranular). The value of C_S reached at steady state is a function of the extent of carburization in the alloy and of the carbon activity in sodium. The carbon activity in sodium is influenced by the nature of the carbon source in the sodium. Thorley and Tyzack [61] observed different values for the carbon concentration reached in type 316L SS specimens after exposure in sodium at 650°C for durations of up to 6 months (Figure 30). They also demonstrated the influence of carbon activity in sodium on the carburization behavior of 316L SS [61].

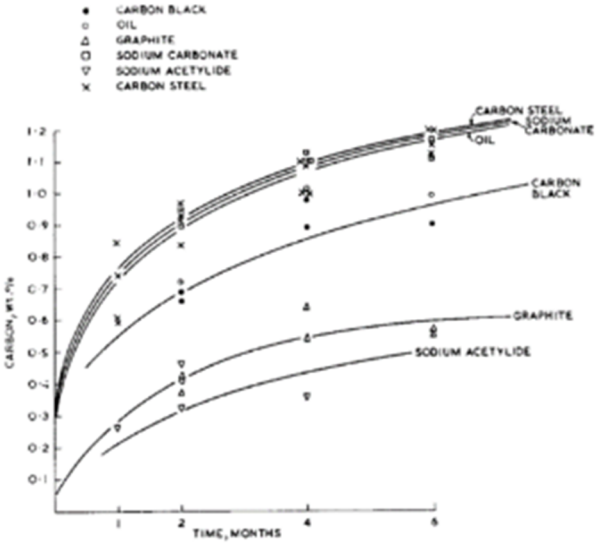

Figure 30. Effect of different carbon sources on the carburization of 316L specimens exposed at 650°C in sodium [61].

To evaluate the carburization kinetics and behavior of materials exposed in liquid sodium, it is essential to know the carbon activity in sodium. Several studies were performed in highly carburizing sodium (with the carbon activity close to or higher than 1), and D_{app} coefficients were extracted. Graphite was used as the carbon source in sodium in Anderson and Sneesby [107] and Dickson et al. [62], while carbon steel was used in the other studies [65, 109, 112]. As mentioned, this method cannot be used to predict the carburization kinetics of a new alloy. In most of the cases, D_{app} was a fitted parameter used to predict the maximum thickness affected by the carburization process. It is obvious that the maximum carburized thickness depends on the material (carbon diffusion coefficient in the matrix and at grain boundaries and the number of precipitated phases (carbides)). Therefore, D_{app} is strongly dependent on the nature of the steel. It cannot be used to predict the carburized thickness of another steel with a different chemical composition and microstructure. Thus, a more accurate lifetime model is needed for considering the carbide precipitation. Such a model was proposed, but it was less accurate at low temperatures where precipitation does not occur according to thermodynamic equilibrium [65, 116]. Furthermore, highly carburizing sodium has been observed only for control rod cladding materials encapsulating B_4C pellets. In general, carburization occurs to a lower extent in SFRs, including in the heat exchanger. This behavior is attributed to the lower carbon activity reached in liquid sodium as a result of the decarburization of constitutive materials in sodium. The observations and results regarding this phenomenon are presented in Section 4.4.2.

4.4.2 Carburization in carburizing sodium (a_c <1)

Carburization of stainless steels was observed when the carbon activity was <1 [94]. The formation of intergranular and intragranular $M_{23}C_6$ carbides was observed near the surface of type 316 SS at 650°C. Type M_6C carbides were also occasionally found attached to the surface of the steel and could have been removed from the steel surface by the flowing sodium. In contrast, ferritic steels were observed to decarburize after exposure to flowing sodium [94]. After exposure in a sodium circuit at 600°C, Fe_3C regions in Fe-2.25Cr-1Mo steel were observed to decompose into carbides of lower carbon activity, such as Cr_7C_3 and Mo_2C. After 2 days at 600°C, the surface of the alloy was observed to be almost completely depleted in carbon.

Conclusions:

- The studies revealed significant carburization of the control rod materials (austenitic and ferritic steels) in close contact with B_4C moderator materials in oxygen-purified liquid sodium above 400 ˚C.
- In low carburization sodium (reactor core and heat exchanger) no significant carburization of austenitic steels was observed. However, significant decarburization of ferritic steels was seen above 600 ˚C in oxygen-purified liquid sodium.

4.5 EFFECT OF SODIUM EXPOSURE ON MECHANICAL PROPERTIES

To quantify the effect of liquid sodium on mechanical properties, a number of tests have been performed including tensile, creep, and fatigue tests. A thorough review has been published [117] and the main findings are reported in this section.

4.5.1 Austenitic steels

For austenitic steels used in the reactor, the effects of corrosion (dissolution and carburization) on mechanical strength have been observed to be negligible in the reactor lifetime, except in the fuel

cladding (strong carburizing conditions). Fuel cladding consists of thinner sections that are more susceptible to carburization [10, 65]. Mass transfer phenomena such as dissolution and deposition observed in the short-term were still observed after 100,000 h exposures for type 304 SS piping materials. A maximum dissolution depth of 30 µm was confirmed without the presence of intergranular or pitting corrosion. All of the high-temperature strengths of type 304 SS materials satisfied the set mechanical values (showing the average strength of as-received materials) [17, 55]. However, some reductions in creep rupture strength and fracture elongation were recognized at high temperatures for ferritic steels, which only became apparent after 500 h exposures [17, 55].

4.5.2 Ferritic steels

The decarburization of ferritic (Grade 22) and FM steels (Grade 91) induced a slight strength decrease at 600°C, as shown in Figure 31.

For ODS FeCr steels, a small amount of mechanical property data can be found in the literature—a compatibility study between ferritic ODS steels and type 316L SS [51]. As mentioned previously, nickel diffused into the ODS steel specimens as a result of dissolution of the 316L loop material. This observation did not affect the UTS of the ODS alloys (Figure 32). Because of these issues, further studies are needed [54, 59].

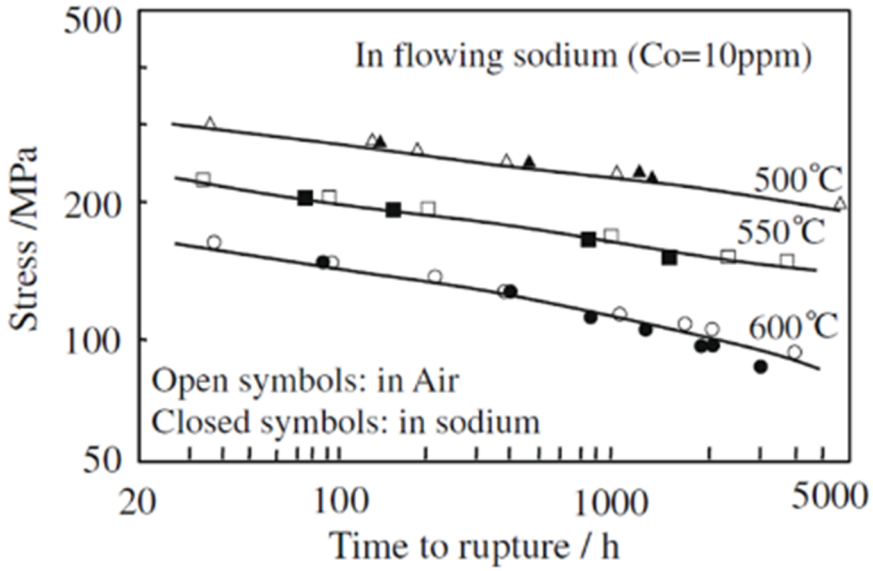

Figure 31. Creep strength of 2.25Cr-1Mo steel exposed for up to 5,000 h in liquid sodium (10 ppm of oxygen) between 500 and 600°C [55].

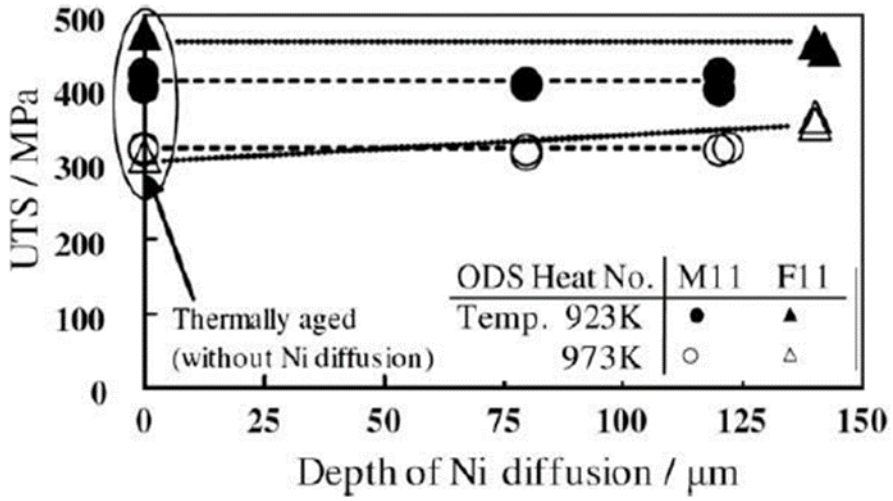

Figure 32. Influence of nickel diffusion on the tensile properties of ferritic ODS steels [54].

Conclusions:
• Dissolution and mass transfer of structural materials in liquid sodium were observed to have a limited effect on the mechanical properties of thick austenitic structural reactor materials (i.e. heat exchangers, reactor vessel). • Dissolution and mass transfer were observed to slightly reduce the strength of ferritic materials in oxygen-purified liquid sodium at 600 ˚C after durations between 1,000 and 5,000 h. • More investigations of thin-walled structures are needed for cladding and compact heat exchangers.

5. CONCLUSIONS

This review of the sodium compatibility literature covers many studies conducted in liquid sodium that produce a general framework for understanding the effects of the sodium environment on the corrosion of structural materials. Such knowledge can be used to inform regulatory decisions of new reactor designs.

- The sodium chemistry was studied after interaction with pure elements and oxygen for up to 1,000 h and for temperatures between 400 and 650°C. In most of the cases the compounds formed between the pure element and the sodium saturated with oxygen were characterized and were mostly oxide compounds (Section 4.2).

- Studies conducted with varied levels of oxygen suggest that to reduce oxidation and dissolution and maximize the lifetime of structural materials (mainly stainless steels) in SFRs, including increasing their safety, the oxygen level in sodium should be monitored and controlled below 1 ppm (Sections 3.2, 3.3.4,4.2, 4.3.1, 4.3.2 and 4.3.5).

- Many studies were specific to one material, mostly steels and limited to a specific set of conditions (static sodium, flowing sodium, carbon activity in sodium, sodium velocity, temperature gradient) (Section 4.3).

- Most flowing sodium TCL and FCL experiments incorporate many different variables in each experiment (Section 4.3.6). More thorough investigations are needed in flowing sodium of integral effects of parameters such as temperature gradient, oxygen content, carbon content, velocity, and dissimilar materials. These fundamental studies would assist in developing predictive models.

- ODS alloys can be very resistant to radiation damage and so are attractive for SFR fuel cladding applications. However, rather limited information has been reported regarding the sodium compatibility of these alloys, including FeCr and FeCrAl variants such as those developed for accident-tolerant LWR [87, 92, 93] (Section 4.3.2).

- Dissolution and mass transfer of structural materials in liquid sodium were observed to have a limited effect on the mechanical properties of thick austenitic structural reactor materials (heat exchangers, reactor vessel; Section 4.5). More investigations of thin-walled structures are needed for cladding and compact heat exchangers.

6. GAP ANALYSIS

The review determined that corrosion models/rates have been developed only for types 316 or 304 austenitic stainless steels in very specific experimental conditions (Section 4.3.4). In general, there is a clear need for better predictive capabilities for sodium compatibility and long-term performance, which would avoid extended experimental campaigns for new materials; design changes; and transient, off-normal, or accident conditions. Models validated by selected experiments would be very useful to designers, operators, and regulators to show how design choices impact reactor lifetime and safety.

- Additional studies are needed to investigate chemical and microstructural changes of pure, binary, ternary and quaternary alloys after exposure to purified and unpurified liquid sodium over a wide range of conditions (static sodium, flowing sodium, carbon activity in sodium, sodium velocity, sodium temperature). These studies would provide necessary information toward the understanding of the corrosion of multi-components alloys in oxygen-purified liquid sodium and liquid sodium saturated with non-metallic impurities such as oxygen or carbon and the development of corrosion models.

- Additional studies are needed across a range of alloy classes (austenitic, ferritic, FM), alloy chemistries (Ni-Cr, Ni-Cr-Fe..), microstructures (e.g., annealed, cold-worked, varied grain sizes), and different conditions (static sodium, flowing sodium, carbon activity in sodium, sodium velocity, temperature gradient). These studies would provide validation data to establish reliable corrosion models.

- Additional studies are needed to understand if there is a critical O content that should be maintained during operation to minimize corrosion for each class of structural alloys. Also, the effect of short-term disruptions in O content of sodium on compatibility has not been evaluated.

- For any new material introduced in an SFR, the corrosion and mechanical behavior after exposure to liquid sodium must be thoroughly studied (chemical, microstructural changes, variation in strength and ductility).

- Models are needed to predict alloy corrosion rates as a function of various reactor condition (temperature, sodium velocity, alloy microstructure, carbon activity, impurities).

- The ability to predict the corrosion rate for a wide range of alloy chemical compositions, including ODS alloys, would be an important tool to aid understanding of future SFR design variations.

- Models are needed to predict the effects of design (e.g., materials selection, temperature) and operating conditions on sodium chemistry, e.g., the uptake of dissolved elements and removal rates by various purification strategies.

- Models are needed to predict the effects of corrosion and sodium chemistry on long-term mechanical properties, including the roles of component thickness and carburization in various alloy classes and microstructures, as mentioned in the literature [117].

REFERENCES

1. Chetal, S.C., et al., *The design of the Prototype Fast Breeder Reactor*. Nuclear Engineering and Design, 2006. **236**(7): p. 852-860.
2. Kütt, M., F. Frieß, and M. Englert, *Plutonium Disposition in the BN-800 Fast Reactor: An Assessment of Plutonium Isotopics and Breeding*. Vol. 22. 2014.
3. Ruggieri, J.-M., et al., *Sodium-Cooled Fast Reactor (SFR). system Safety Assessment*, in *GEN IV International Forum. Revision 1*. 2017.
4. Hejzlar, P., et al., *Terrapower, LLC Traveling wave reactor development program overview*. Nuclear Engineering and Technology, 2013. **45**(6): p. 731-744.
5. Hitachi. *PRIMS reactor*. 01\29\2019; Available from: https://nuclear.gepower.com/build-a-plant/products/nuclear-power-plants-overview/prism1.
6. *TerraPower and GE Hitachi Nuclear Energy Introduce Commercial Natrium™ Power Production and Storage System*. 12/04/2020]; Available from: https://www.terrapower.com/terrapower-and-ge-hitachi-nuclear-energy-launch-natrium-technology/.
7. Xu, M., *The status and prospects of fast reactor technology development in china*. Engineering Science, 2008. **10**(1): p. 70-76.
8. Kim, Y., et al., *Design Concept of Advanced Sodium-Cooled Fast Reactor and Related R&D in Korea*. Science and Technology of Nuclear Installations, 2013. **2013**: p. 18.
9. Reuters. *France drops plans to build sodium-cooled nuclear reactor*. 2019 August 30, 2019 [cited 2021 January 22, 2021]; Available from: https://www.reuters.com/article/us-france-nuclearpower-astrid/france-drops-plans-to-build-sodium-cooled-nuclear-reactor-idUSKCN1VK0MC.
10. Yoshida, E. and T. Furukawa, *21 - Corrosion issues in sodium-cooled fast reactor (SFR) systems*, in *Nuclear Corrosion Science and Engineering*, D. Féron, Editor. 2012, Woodhead Publishing. p. 773-806.
11. Diercks, D.R., *Structural materials for breeder reactor cores and coolant circuits*. 1984: United States.
12. Foust, O.J., *Sodium-NaK Engineering Handbook*. Vol. Volume I Sodium chemistry and physical properties. 1972, United States: 1972.
13. Fink, J. and L. Leibowitz, *Calculation of thermophysical properties of sodium.[LMFBR]*. 1981, Argonne National Lab., IL (USA).
14. Gnanasekaran, T., R.K. Dayal, and B. Raj, *10 - Liquid metal corrosion in nuclear reactor and accelerator driven systems*, in *Nuclear Corrosion Science and Engineering*, D. Féron, Editor. 2012, Woodhead Publishing. p. 301-328.
15. Sridharan, R., et al., *An electrochemical hydrogen meter for measuring hydrogen in sodium using a ternary electrolyte mixture*. Journal of Nuclear Materials, 2003. **312**(1): p. 10-15.
16. Sylvia, J.I., et al., *Development of sodium leak detectors for PFBR*. Nuclear Engineering and Design, 2012. **249**: p. 419-431.
17. U. Borgstedt, H. and G. Frees, *Liquid Metal Systems: Material Behavior and Physical Chemistry in Liquid Metal Systems 2*. 1995.
18. Mathews, C.K., *Liquid sodium—The heat transport medium in fast breeder reactors*. Bulletin of Materials Science, 1993. **16**(6): p. 477-489.
19. Borgstedt, H.U. and C.K. Mathews, *Applied chemistry of the alkali metals*. 1987: Plenum Press.
20. Zhao, F. and X. Ren, *Optimal performance analysis of a sodium cold trap*. Nuclear Engineering and Design, 2009. **239**(3): p. 490-494.
21. Kozlov, F.A., et al., *Studies validating a sodium purification system for fast reactors*. Atomic Energy, 2012. **112**(1): p. 21-28.
22. Hobdell, M.R. and C.A. Smith, *Electrochemical techniques for monitoring dissolved carbon, hydrogen and oxygen in liquid sodium*. Journal of Nuclear Materials, 1982. **110**(2): p. 125-139.
23. Longson, B. and A.W. Thorley, *Solubility of carbon in sodium*. Journal of Applied Chemistry, 1970. **20**(12): p. 372-379.
24. Ainsley, R., et al., *The solubility of carbon in sodium*. Journal of Nuclear Materials, 1974. **52**(2): p. 255-276.

25. Gehri, D.C., *The Behavior of Carbon in Liquid Sodium. U. S. Atomic Energy Commision*. 1970, Report AI-AEC-12826, 1970.
26. Salzano, F.J. and L. Newman, *Electrochemical measurement of the solubility of carbon in sodium.* Nuclear Technology, 1972. **13**(3): p. 289-296.
27. Johnson, G.K., et al., *Enthalpy of formation of disodium acetylide and of monosodium acetylide at 298.15 k, heat capacity of disodium acetylide from 5 to 350 k, and some derived thermodynamic properties.* The Journal of Chemical Thermodynamics, 1973. **5**(1): p. 57-71.
28. Romedenne, M., *Carburization and boriding of stainless steels in liquid sodium: chemical interaction between the control rods and B4C pellets*. 2018, Toulouse INP.
29. Addison, C.C., et al., *The Alkali-Metals.* The Chemical Society, International Symposium on the Alkali Metals, 1967. **460**(Pub. No. 22).
30. Vissers, D.R., et al., *A Hydrogen-Activity Meter for Liquid Sodium and Its Application to Hydrogen Solubility Measurements.* Nuclear Technology, 1974. **21**(3): p. 235-244.
31. Noden, J.D., *A general equation for the solubility of oxygen in liquid sodium*. 1972: United Kingdom. p. 18.
32. Wriedt, H.A., *The Na-O (Sodium-Oxygen) System.* Bulletin of Alloy Phase Diagrams, 1987. **8**(3): p. 234-246.
33. Cramer, S.D. and B.S. Covino, Jr., *20.1.1 Dissolution*, in *ASM Handbook, Volume 13A - Corrosion: Fundamentals, Testing, and Protection*. ASM International.
34. Barker, M.G. and D.J. Wood, *THe corrosion of chromium, iron, and stainless steel in liquid sodium.* Journal of the Less Common Metals, 1974. **35**(2): p. 315-323.
35. Rivollier, M., *Corrosion des aciers austénitiques par le sodium liquide en présence d'oxygène*. 2017.
36. Fredrickson, D.R. and M.G. Chasanov, *The enthalpy of sodium oxide Na2O to 1300 K by drop calorimetry.* The Journal of Chemical Thermodynamics, 1973. **5**(4): p. 485-490.
37. Bin Jenn, S., P.C.S. Wu, and P. Chiotti, *Thermodynamic properties of the double oxides of Na2O with the oxides of Cr, Ni and Fe.* Journal of Nuclear Materials, 1977. **67**(1): p. 13-23.
38. Bhat, N.P. and H.U. Borgstedt, *Thermodynamic stability of Na4FeO3 and threshold oxygen levels in sodium for the formation of this compound on AISI 316 steel surfaces.* Journal of Nuclear Materials, 1988. **158**: p. 7-11.
39. Selle, V.A. and D.L. Olson, *Materials Considerations in Liquid Systems in Power Generation*, in *NACE*, G.A. Whitlow and N.J. Hoffman, Editors. 1978: Houston, Texas,. p. 15–22.
40. Cramer, S.D. and B.S. Covino, Jr., *Corrosion: Fundamentals, Testing, and Protection*. 2003: ASM International.
41. Zebroski, E., et al., *Effects of mass transfer, and of changes in properties, on austenitic steels in flowing sodium*. 1967: p. 195-211.
42. Thorley, A.W. and J.A. Bardsley, *Structural changes in materials exposed to liquid sodium.* Journal of the Royal Microscopical Society, 1968. **88**(4): p. 431-447.
43. Weeks, J.R. and H.S. Isaacs, *Corrosion and Deposition of Steels and Nickel-Base Alloys in Liquid Sodium*, in *Advances in Corrosion Science and Technology*, M.G. Fontana and R.W. Staehle, Editors. 1973, Springer US: Boston, MA. p. 1-66.
44. Baque, P., et al., *Contribution a l'etude de la corrosion de l'acier austenitique bas carbone (afnor Z3 CN 18-10) par le sodium liquide a 700°C*. Vol. 54. 1974. 241-244.
45. Kolster, B.H., *Mechanism of Fe and Cr transport by liquid sodium in non-isothermal loop systems.* Journal of Nuclear Materials, 1975. **55**(2): p. 155-168.
46. Nevzorov, B.A., et al., *Corrosion of structural materials in liquid alkali metals*. 1977.
47. Tyzack, C. and A.W. Thorley, *Review of corrosion and carbon transport behaviour of ferritic materials exposed to sodium*. 1978, United Kingdom: British Nuclear Energy Society.
48. Suzuki, T., et al., *Sodium corrosion behavior of austenitic alloys and selective dissolution of chromium and nickel.* Journal of Nuclear Materials, 1986. **139**(2): p. 97-105.
49. Suzuki, T. and I. Mutoh, *The downstream effect in the corrosion of metallic materials in a type 316 stainless steel sodium loop system.* Journal of Nuclear Materials, 1986. **140**(1): p. 56-62.
50. Karpov, A.V., et al., *Compatibility of Structural Materials with Sodium According to Data from the Experience Gained in 40 Years of Operation of the BR-5/BR-10 Reactor.* Atomic Energy, 2001. **91**(5): p. 951-955.

51. Gnanasekaran, T. and C.K. Mathews, *Threshold oxygen levels in sodium necessary for the formation of NaCrO2 in sodium-steel systems.* Journal of Nuclear Materials, 1986. **140**(3): p. 202-213.
52. Ganesan, V. and V. Ganesan, *Corrosion of annealed AISI 316 stainless steel in sodium environment.* Journal of Nuclear Materials, 1998. **256**(1): p. 69-77.
53. Ganesan, V., V. Ganesan, and H.U. Borgstedt, *Analysis of CREVONA sodium loop material.* Journal of Nuclear Materials, 2003. **312**(2): p. 174-180.
54. Yoshida, E. and S. Kato, *Sodium compatibility of ODS steel at elevated temperature.* Journal of Nuclear Materials, 2004. **329-333**: p. 1393-1397.
55. Furukawa, T., S. Kato, and E. Yoshida, *Compatibility of FBR materials with sodium.* Journal of Nuclear Materials, 2009. **392**(2): p. 249-254.
56. Ohtsuka, S., et al., *Model calculation of Cr dissolution behavior of ODS ferritic steel in high-temperature flowing sodium environment.* Journal of Nuclear Materials, 2018. **505**: p. 44-53.
57. Rivollier, M., et al., *Oxidation of 316L(N) stainless steel in liquid sodium at 650 °C.* Journal of Nuclear Materials, 2018. **500**: p. 337-348.
58. Chopra, O.K., K. Natesan, and T.F. Kassner, *Carbon and nitrogen transfer in Fe-9 Cr-Mo ferritic steels exposed to a sodium environment.* Journal of Nuclear Materials, 1981. **96**(3): p. 269-284.
59. Asayama, T., T. Furukawa, and E. Yoshida, *Evaluation procedure for sodium environmental effects on 316FR and modified 9Cr-1Mo steel for the structural design of Japanese fast breeder reactors.* Vol. 391. 1999. 61-66.
60. Snyder, R.B., K. Natesan, and T.F. Kassner, *Kinetics of the carburization-decarburization process of austenitic stainless steels in sodium.* Journal of Nuclear Materials, 1974. **50**(3): p. 259-274.
61. Thorley, A. and C. Tyzack. *Carburisation of stainless steels in sodium containing carbon impurities and its effect on mechanical properties.* in *British Nuclear Energy Society*. 1971.
62. Dickson, J., et al., *Carburisation of stainless steel immersed in carbon-contaminated sodium: a new technique for estimating the diffusion coefficients.* 1988, France: Societe Francaise d'Energie Nucleaire.
63. Rademakers, P.L.F. and B.H. Kolster, *Corrosion of various ferritic steels in an isothermal sodium loop system.* Journal of Nuclear Materials, 1981. **97**(3): p. 309-318.
64. Romedenne, M., et al., *Carburization of austenitic and ferritic stainless steels in liquid sodium: Comparison between experimental observations and simulations.* Corrosion Science, 2019. **159**: p. 108147.
65. Romedenne, M., et al., *Carburization of Austenitic and Ferritic Steels in Carbon-Saturated Sodium: Preliminary Results on the Diffusion Coefficient of Carbon at 873 K.* Oxidation of Metals, 2017. **87**(5): p. 643-653.
66. Saltelli, A., O.K. Chopra, and K. Natesan, *An assessment of carburization-decarburizatton behaviour of Fe-9Cr-Mo steels in a sodium environment.* Journal of Nuclear Materials, 1982. **110**(1): p. 1-10.
67. Chopra, O.K., et al., *Liquid-Metal Corrosion.* Fusion Technology, 1985. **8**(2P1): p. 1956-1969.
68. Charnock, W., et al., *Effect of high carbon activity sodium upon the mechanical properties of AISI 316 stainless steel.* 1975, Central Electricity Generating Board, Berkeley (UK) Berkeley Nuclear Labs. Physical metallurgy of reactor fuel elements: United Kingdom: Metals Society.
69. Courouau, J., et al. *Corrosion by liquid sodium of materials for sodium fast reactors: the CORRONa testing device.* in *International Congress on Advances in Nuclear Power Plants*. 2011.
70. Addison, C., M. Barker, and D.J.J.o.t.C.S. Wood, Dalton Transactions, *The role of dissolved oxygen in the corrosion of niobium and tantalum by liquid sodium.* 1972(1): p. 13-16.
71. Barker, M.G. and C.W. Morris, *The corrosion of molybdenum and tungsten in liquid sodium.* Journal of the Less Common Metals, 1976. **44**: p. 169-176.
72. Pawel, S.J., *Compatibility Assessment of Advanced Stainless Steels in Sodium.* Fusion Science and Technology, 2012. **61**(1T): p. 369-374.
73. Pint, B.A., et al., *Re-establishing the paradigm for evaluating halide salt compatibility to study commercial chloride salts at 600°C–800°C.* Materials and Corrosion, 2019. **70**(8): p. 1439-1449.
74. Raiman, S.S., et al., *Amorphous and partially-amorphous metal coatings for corrosion resistance in molten chloride salt.* Solar Energy Materials and Solar Cells, 2019. **201**: p. 110028.
75. Tortorelli, P.F. and S.J. Pawel, *Corrosion by Liquid Metals*, in *Corrosion: Fundamentals, Testing, and Protection*. 2003, ASM International. p. 0.

76. International Atomic Energy Agency, V., *Alkali Metal Coolants Proceedings of the Symposium on Alkali Metal Coolants - Corrosion Studies and System Operating Experience*. 1967, International Atomic Energy Agency (IAEA): IAEA.
77. Rademakers, P. and B.J.J.o.N.M. Kolster, *Corrosion of various ferritic steels in an isothermal sodium loop system.* 1981. **97**(3): p. 309-318.
78. Yoshida, E., S. Kato, and Y. Wada, *Post-Corrosion and Metallurgical Analyses of Sodium Piping Materials Operated for 100,000 Hours*, in *Liquid Metal Systems: Material Behavior and Physical Chemistry in Liquid Metal Systems 2*, H.U. Borgstedt and G. Frees, Editors. 1995, Springer US: Boston, MA. p. 55-66.
79. Sivai Bharasi, N., et al., *Effect of flowing sodium on corrosion and tensile properties of AISI type 316LN stainless steel at 823 K.* Journal of Nuclear Materials, 2008. **377**(2): p. 378-384.
80. Bharasi, N.S., et al., *Microstructure, corrosion and mechanical properties characterization of AISI type 316L(N) stainless steel and modified 9Cr-1Mo steel after 40,000 h of dynamic sodium exposure at 525 °C.* Journal of Nuclear Materials, 2019. **516**: p. 84-99.
81. Li, M.M., K. Natesan and W.Y. Chen, *Understanding and Predicting Effect of Sodium Exposure on Microstructure of Grade 91 Steel.* ANL Technical Report, 2017. **osti_1409210**.
82. Borgstedt, H.U., et al., *Sodium Loops for Material Behavior Testing In Flowing Sodium in KFK*, in *Material Behavior and Physical Chemistry in Liquid Metal Systems*, H.U. Borgstedt, Editor. 1982, Springer US: Boston, MA. p. 185-191.
83. Barker, M.G. and D.J. Wood, *The role of dissolved oxygen in the corrosion of titanium and zirconium by liquid sodium.* Journal of the Chemical Society, Dalton Transactions, 1972(22): p. 2451-2454.
84. Barker, M.G., *The reactions of the liquid alkali metals with the metals Zr, Nb, Ta, Mo and W and their oxides.* Revue Internationale des Hautes Temperatures et des Refractaires, 1979. **16**(3): p. 237-243.
85. Noda, T. and T. Suzuki, *The corrosion of vanadium and vanadium-base binary alloys in oxygen-saturated liquid sodium.* Corrosion Science, 1976. **16**(7): p. 413-422.
86. Hodkin, E.N., D.A. Mortimer, and M. Nicholas, *The wetting of some ferrous materials by sodium*. 1973, United Kingdom: British Nuclear Energy Society.
87. Massey, C.P., et al., *Microstructural evaluation of a Fe-12Cr nanostructured ferritic alloy designed for impurity sequestration.* Journal of Nuclear Materials, 2019. **522**: p. 111-122.
88. Massey, C.P., et al., *Multiscale investigations of nanoprecipitate nucleation, growth, and coarsening in annealed low-Cr oxide dispersion strengthened FeCrAl powder.* Acta Materialia, 2019. **166**: p. 1-17.
89. Li, N., et al., *Oxide Morphology of a FeCrAl Alloy, Kanthal APMT, Following Extended Aging in Air at 300 °C to 600 °C.* Metallurgical and Materials Transactions A, 2018. **49**(7): p. 2940-2950.
90. Jun, J., et al., *Compatibility of FeCrAlMo with flowing PbLi at 500°-650 °C.* Journal of Nuclear Materials, 2020. **528**: p. 151847.
91. Kano, S., et al., *Sodium Compatibility of Ceramics*, in *Liquid Metal Systems: Material Behavior and Physical Chemistry in Liquid Metal Systems 2*, H.U. Borgstedt and G. Frees, Editors. 1995, Springer US: Boston, MA. p. 85-94.
92. Yamamoto, Y., et al., *Development and property evaluation of nuclear grade wrought FeCrAl fuel cladding for light water reactors.* Journal of Nuclear Materials, 2015. **467**: p. 703-716.
93. Hoelzer, D.T., et al., *Modern nanostructured ferritic alloys: A compelling and viable choice for sodium fast reactor fuel cladding applications.* Journal of Nuclear Materials, 2020. **529**: p. 151928.
94. Thorley, A.W. and C. Tyzack, *Corrosion Behaviour of Steels and Nickel Alloys in High-Temperature Sodium.* 1967, IAEA: International Atomic Energy Agency (IAEA).
95. Borgstedt, H.U., G. Drechsler, and G. Frees, *Influence of the Surface Quality on the Liquid Sodium Corrosion of Nickel Alloys*. 1967, International Atomic Energy Agency (IAEA): IAEA.
96. Natesan, K., O.K. Chopra, and T.F. Kassner, *Compatibility of Fe–2¼ wt% Cr–1 wt% Mo Steel in a Sodium Environment.* Nuclear Technology, 1976. **28**(3): p. 441-451.
97. Shiels, S., et al., *Characterization of the sodium corrosion behavior of commercial austenitic steels.* 1980, Westinghouse Electric Corp., Madison, PA (USA). Advanced Reactors Div ….
98. Thorley, A.W., A. Blundell, and J.A. Bardsley, *Mass Transfer of Stainless Steel in Pumped Sodium Loops and its Effect on Microstructure*, in *Material Behavior and Physical Chemistry in Liquid Metal Systems*, H.U. Borgstedt, Editor. 1982, Springer US: Boston, MA. p. 5-18.

99. Khatak, H.S., et al., *Variation in the Tensile Properties of Aisi 316 Stainless Steel on Exposure to High Carbon Dynamic Sodium at 723 K*, in *Liquid Metal Systems: Material Behavior and Physical Chemistry in Liquid Metal Systems 2*, H.U. Borgstedt and G. Frees, Editors. 1995, Springer US: Boston, MA. p. 121-126.
100. Bharasi, N.S., et al., *Evaluation of microstructural, mechanical properties and corrosion behavior of AISI type 316LN stainless steel and modified 9Cr-1Mo steel exposed in a dynamic bimetallic sodium loop at 798 K (525 C) for 16,000 hours.* 2012. **43**(2): p. 561-571.
101. Prasanthi, T.N., et al., *Modification in the Microstructure of Mod. 9Cr-1Mo Ferritic Martensitic Steel Exposed to Sodium.* Metallurgical and Materials Transactions A, 2014. **45**(10): p. 4220-4234.
102. Pillai, S.R., et al., *Corrosion behavior and tensile properties of AISI 316LN stainless steel exposed to flowing sodium at 823 K.* Journal of Materials Engineering and Performance, 2000. **9**(1): p. 98-102.
103. Sudha, C., et al., *Carburization behavior of AISI 316LN austenitic stainless steel - Experimental studies and modeling.* Journal of Nuclear Materials, 2010. **402**(2-3): p. 186-195.
104. Bharasi, N.S., et al., *Microstructure, corrosion and mechanical properties characterization of AISI type 316L (N) stainless steel and modified 9Cr-1Mo steel after 40,000 h of dynamic sodium exposure at 525° C.* 2019. **516**: p. 84-99.
105. Zhang, J., P. Hosemann, and S. Maloy, *Models of liquid metal corrosion.* Journal of Nuclear Materials, 2010. **404**(1): p. 82-96.
106. Zhang, J., T.F. Marcille, and R. Kapernick, *Theoretical Analysis of Corrosion by Liquid Sodium and Sodium-Potassium Alloys.* CORROSION, 2008. **64**(7): p. 563-573.
107. Anderson, W. and G. Sneesby, *Carburization of austenitic stainless steel in liquid sodium.* 1960, Atomics International. Div. of North American Aviation, Inc., Canoga Park ….
108. Natesan, K. and T.F. Kassner, *Thermodynamic and kinetic aspects of carbon transport in sodium-steel systems.* Journal of Nuclear Materials, 1970. **37**(2): p. 223-235.
109. Gwyther, J.R., M.R. Hobdell, and A.J. Hooper, *Carburization of austenitic and ferritic alloys in carbon-saturated sodium at 916 K.* Metals Technology, 1974. **1**(1): p. 406-411.
110. Nishio, G. and J.J.J.o.N.M. Shimokawa, *Kinetics of carbon transfer governing compatibility between uranium carbide and stainless steel bonded with sodium.* 1973. **47**(1): p. 87-94.
111. Ito, T., et al., *Evaluation of Carburization and Decarburization Behavior of Fe-9Cr-Mo Ferritic Steels in Sodium Environment.* Journal of Nuclear Science and Technology, 1992. **29**(4): p. 367-377.
112. W. Thorley and M. R. Hobdell, U.N.d.r., ND-R-983 (1984). *Carbon in sodium: a review.* UKAEA Northern division report, 1984. **ND-R-983**.
113. Wagner, C., *Reaktionstypen bei der Oxydation von Legierungen.* Zeitschrift fur Elektrochemie, 1959. **63**(7): p. 772-790.
114. Thorley, A. and M. Hobdell, *Carbon in sodium-A review of work in the UK.* 1980.
115. Crank, J., *The Mathematics of Diffusion.* 1956, Oxford: Clarendon Press. 402.
116. Romedenne, M., et al., *Carburization of austenitic and ferritic stainless steels in liquid sodium: comparison between experimental observations and simulations.* Corrosion Science, 2019, **159**: p.108147.
117. Natesan, K., et al., *Sodium effects on mechanical performance and consideration in high temperature structural design for advanced reactors.* Journal of Nuclear Materials, 2009. **392**(2): p. 243-248.